# UC Santa Barbara

## UC Santa Barbara Electronic Theses and Dissertations

### Title

III-nitride microLEDs down to 1-micron diameter

### Permalink

https://escholarship.org/uc/item/8z76k4w9

### Author

Smith, Jordan M.

### Publication Date

2023

Peer reviewed|Thesis/dissertation

eScholarship.org Powered by the California Digital Library
University of California

UNIVERSITY OF CALIFORNIA

Santa Barbara

# III-nitride microLEDs down to 1-micron diameter

A dissertation submitted in partial satisfaction

of the requirements for the degree

Doctor of Philosophy

in Materials

by

Jordan M. Smith

Committee in charge:

Professor Steven P. DenBaars, Chair

Professor Shuji Nakamura

Professor James S. Speck

Professor Michael J. Gordon

December 2023

The dissertation of Jordan M. Smith is approved.

---

Shuji Nakamura

---

James S. Speck

---

Michael J. Gordon

---

Steven P. DenBaars, Committee Chair

September 2023

III-nitride microLEDs down to 1-micron diameter

Copyright © 2023

by

Jordan M. Smith

**Jordan M. Smith** Curriculum Vitae January 2023

Email: jordan@msmithphd.com
LinkedIn: linkedin.com/in/jormsmith/
Google Scholar: scholar.google.com/citations?hl=en&user=61QjdFsAAAAJ

## EDUCATION

**University of California, Santa Barbara**

Doctor of Philosophy, Materials — Sep 2017 – present

- PhD Advisor: Prof. Steven P. DenBaars
- PhD Committee: Prof. Shuji Nakamura, Prof. James S. Speck, Prof. Steven P. DenBaars, and Prof. Michael J. Gordon
- Dissertation Topic: Process Development, Characterization, and Modeling of III-Nitride microLEDs Down to 1-micron in Diameter

**University of Washington, Seattle**

*Master of Science*, Materials Science and Engineering — 2017

- MS Thesis: Increasing Electron and Hole Wavefunction Overlap through Quadratic Compositional Modulation in III-Nitride Multiple Quantum Wells

Bachelor of Science, Materials Science and Engineering — 2016

## WORK EXPERIENCE

**Solid-State Lighting & Energy Electronics Center** — Santa Barbara, CA

microLED PhD Researcher — Sep 2017 – present

*Semiconductor processing and fabrication*

- Overcame limitations of lithography—a common roadblock in semiconductor technology—to fabricate 1μm microLEDs through a self-aligned technique that leverages unique chemical selectivities of III-Nitrides
- Reduced microLED production times and increased yield by lowering the standard number of 4 lithography steps to 3 whilst simultaneously eliminating errors caused by misalignment
- Increased microLED efficiency (EQE) over 50% by removing impurities on the sidewall and passivating non-radiative Ga-atom dangling bonds through a sequence of chemical treatments
- Developed processes for multiple optoelectronic / photonic devices, including lasers, LEDs, and a meta-lens

*Optical metrology and characterization*

- Calibrated spectrometer wavelength (diffractive grating) for all visible colors using a Mercury-Argon source
- Radiometrically calibrated the system to measure spectral flux, W/nm, with a power resolution below *100 picowatts* to detect low signal emitted from 1μm microLEDs driven below *0.1A/cm^2*
- Programmed multi-user LabVIEW acquisition interface with hardware with advanced features, including: hierarchical data saving structure | savable user configurations | conditional adjustments & safety controls
- Coded algorithms to calculate radiometric and photometric quantities (e.g., EQE/lumens vs. current density) and visualize them real-time in the LabVIEW UI, using a Python integration for complex calculations
- Incorporated flexibility for multiple experimental conditions such as inverting the integrating sphere to measure flip-chip or top-emitting device geometries

*Optical modeling*

- Verified experimental results with modeling: Simulated sidewall reflections inside microLED mesas to explain unexpected increases in efficiency from 2.5% to 5% as diameter shrank from 50μm to 1μm in red III-Nitride microLEDs
- Merged wave and non-sequential optics models (Lumerical FDTD and LightTools) to describe processes occurring at differing length-scales in a self-consistent model—presented at ICNS 2019

**Meta** (Oculus / Facebook Reality Labs) Cork, Ireland

microLED Research Intern (manager: Céline Oyer) Jul 2017 – Sep 2017

- Explored novel applications of III-Nitride and conventional III-V microLEDs using electrical and thermal atomic force microscopy (AFM) for augmented reality technology development—NDA censored

**III-Nitride AlGaN UV LED Lab (Chichibu Group)** Sendai, Japan

Visiting Researcher, Tohoku University Apr 2016 – Sep 2016

- Improved AlGaN LED epitaxy structure's wavefunction overlap from 27% to 93% by using a Schrodinger-Poisson solver to optimize interconnected band structure, piezoelectric strain effects, and Al composition
- Measured recombination lifetimes in ultraviolet LEDs using cathodoluminescence spectroscopy (CL) and low-temperature time-resolved photoluminescence (TRPL) to compare real-world results with the model

**Carbon-Fiber Manufacturer (Hexcel)** Seattle, WA

Quality Engineering Intern Jun 2015 – Sep 2015

- Reduced manufacturing costs up to $20,000/month by pinpointing the root cause of failure in a carbon-fiber part production line by using VBA programming to analyze yield statistics

**BS/MS Research (University of Washington)** Seattle, WA

Gallium Oxide Thin-film Research (Ohuchi Group) Sep 2015 – Mar 2016

- Fit optical dispersion curves from ellipsometry of $Ga_xAl_{(1-x)2}O_3$ compositional spread films to calculate the Abbe number
- Synthesized Ga2O3 films via pulsed laser deposition (PLD)

Thermoelectric materials research (Jen Group) Feb 2014 – Jun 2015

- Analyzed structure of pnictogen chalcogenide nanoparticles using SEM and TEM
- Developed a solvothermal synthetic pathway to grow novel core shell $Bi_2Te_3/Bi_2Se_3$ nanoparticles
- Examined how to control nanostructure of Bismuth Telluride and its effects on thermal and electrical transport properties

ADDITIONAL EXPERIENCE, PROJECTS, & EXTRACURRICULARS

**MOCVD Teaching Assistant** Santa Barbara, CA

TA for graduate level MOCVD course Apr 2021 – Jun 2021

- Lead class discussions, planned course material, and designed problems for MOCVD class on epitaxial growth of optoelectronic materials
- Topics included reactor design, flow mechanics, kinetics, growth mechanisms, and precursor chemistry

**New Venture Competition** Santa Barbara, CA

Startup Competition Finalist Nov 2018 – May 2019

- Analyzed technological trends to develop, refine and validate a startup microLED printing business model while collaborating with a multidisciplinary team of 4 (marketing, technology management, engineering)
- Won the Impact Award and $5000 and placed 6th after pitching our business to an investor panel in the final round, after progressing through multiple stages of the competition beginning with over 100 teams

**Characterization of Si as an Li-Ion Anode Material** Seattle, WA

Undergraduate Senior-year Team Project Sep 2015 – Mar 2016

- Characterized structure, morphology and composition of silicon powders using SEM, XPS, FTIR, XRD and light scattering particle size analysis to successfully determine which properties affected electrochemical performance in Li-ion batteries using silicon
- Proposed a detailed research plan for my team with the approval of EnerG2 to meet deadlines set by the company and complete the project within 2 quarters

**Piezoelectric Energy Harvesting Shoe** Seattle, WA

Junior-Year Team Project Jan 2015 – Jun 2015

- Wrote a research grant proposal for the creation and characterization of a shoe integrated with a piezoelectric transducer to harvest energy from human footsteps
- Designed an energy harvesting circuit using a bridge rectifier to convert AC current produced by the piezoelectric transducer to DC current
- Tested fatigue life and fracture toughness of PZT and PVDF piezoelectric elements
- Tested the power output of the energy harvesting device by simulating human footsteps using cyclic compressive loading

**Defect Characterization in Composite Aircraft** Seattle, WA

Junior-Year Boeing Collaboration Project Sep 2014 – Dec 2014

- Fabricated prepreg carbon-fiber composite panels with varying degrees of porosity to analyze the effects of porosity on mechanical strength
- Performed ASTM standard tensile strength tests on carbon-fiber panels to determine their yield point
- Calculated the maximum percent porosity allowable in carbon-fiber composites to prevent mechanical failure in a commercial aircraft

## SKILLS

*Coding:*

- LabVIEW
- Python
- MATLAB

*Visualization Software:*

- Origin / OriginPro
- Matplotlib / Seaborn
- Excel

*Modeling:*

- LightTools: geometric non-sequential ray tracing
- Lumerical FDTD: wave-based optical modeling by solving Maxwell's equations
- Lumerical STACK: Analytical transfer-matrix solver for planar thin-film structures
- Nextnano: Schrodinger-Poisson solver for modeling bandstructure, transport, and quantum effects in semiconductor heterostructures

*Semiconductor Device Fabrication and Processing:*

Lithography:

- Stepper
- Contact Aligner
- Mask Design (Tanner L-edit)

Etch:

- Reactive Ion (RIE)
- Inductively Coupled Plasma (ICP)
- Wet Etch
- Vapor HF
- Selective III-Nitride etching

Deposition:

- Sputter
- Electron beam
- Ion beam
- Atomic Layer Deposition (ALD)
- Plasma-enhanced chemical vapor deposition (PECVD)

Other:

- Dicing saw
- Rapid thermal annealing (RTA)

*Materials Characterization:*

- Scanning electron microscopy (SEM)
- Optical microscopy
- Atomic force microscopy (AFM)
- Ellipsometry
- Focused ion beam (FIB)
- Profilometry
- Sheet resistance (4-point probe)
- Confocal laser scanning
- Cathodoluminescence spectroscopy (CL)
- Time-resolved photoluminescence spectroscopy (TRPL, PL)

*Device Testing, Metrology, Characterization:*

- Diode power-current-voltage (LIV, IV)
- Integrating spheres
- Charge coupled devices (CCD)
- Photometry / Radiometry
- Radiometric power calibrations
- Spectrometer / monochrometer
- Optical fibers
- Photodiodes
- Color science

## HONORS & AWARDS

- Solid-State Lighting & Energy Electronics Center (SSLEEC) Outstanding Graduate Student Achievement Award (x3) 2019, 2021, 2022
- NSF GRFP: National Science Foundation Graduate Research Fellowship Program 2017-2022
- New Venture Competition Finalist and Impact Award 2019
- Individualized Professional Skills (IPS) Grant 2019
- GO! Scholarship (visiting researcher support, Tohoku University) 2016
- Freeman-Asia Scholarship (research-abroad support) 2016
- Pfeiffer Scholarship (departmental honors) 2015
- Mary Gates Research Scholarship (for undergraduate research) 2014

## PUBLICATIONS, PATENTS, & PRESENTATIONS

### Journal Articles

(1) Ewing, J.; Lynsky, C.; Zhang, J.; Shapturenka, P.; Wong, M.; **Smith, J. M.**; Iza, M.; Speck, J. S.; Denbaars, S. P. Influence of Superlattice Structure on V-Defect Distribution, External Quantum Efficiency and Electroluminescence for Red InGaN Based MLEDs on Silicon. *Crystals* **2022**, *12* (9), 1216. https://doi.org/10.3390/cryst12091216.

(2) Rienzi, V.; **Smith, J. M.**; Lim, N.; Chang, H.-M.; Chan, P.; Wong, M. S.; Gordon, M. J.; Denbaars, S. P.; Nakamura, S. Demonstration of III-Nitride Red LEDs on Si Substrates via Strain-Relaxed Template by InGaN Decomposition Layer. *Crystals* **2022**, *12* (8), 1144. https://doi.org/10.3390/cryst12081144.

(3) Ley, R. T.; **Smith, J. M.**; Wong, M. S.; Margalith, T.; Nakamura, S.; DenBaars, S. P.; Gordon, M. J. Revealing the Importance of Light Extraction Efficiency in InGaN/GaN MicroLEDs via Chemical Treatment and Dielectric Passivation. *Applied Physics Letters* **2020**, *116*, 251104. https://doi.org/10.1063/5.0011651.

(4) Wong, M. S.; Kearns, J. A.; Lee, C.; **Smith, J. M.**; Lynsky, C.; Lheureux, G.; Choi, H.; Kim, J.; Kim, C.; Nakamura, S.; Speck, J. S.; DenBaars, S. P. Improved Performance of AlGaInP Red Micro-Light-Emitting Diodes with Sidewall Treatments. *Opt. Express* **2020**, *28* (4), 5787. https://doi.org/10.1364/OE.384127.

(5) **Smith, J. M.**; Ley, R.; Wong, M. S.; Baek, Y. H.; Kang, J. H.; Kim, C. H.; Gordon, M. J.; Nakamura, S.; Speck, J. S.; DenBaars, S. P. Comparison of Size-Dependent Characteristics of Blue and Green InGaN MicroLEDs down to 1Mm in Diameter. *Appl. Phys. Lett.* **2020**, *116* (7), 071102. https://doi.org/10.1063/1.5144819.

(6) Mohtashami, Y.; Heki, L. K.; Wong, M. S.; **Smith, J. M.**; Ewing, J. J.; Mitchell, W. J.; Nakamura, S.; DenBaars, S. P.; Schuller, J. A. Metasurface Light-Emitting Diodes with Directional and Focused Emission. **2023**, No. *Preparing Manuscript*.

(7) **Smith, J. M.**; Panpan, L.; Wong, M. S.; Ley, R. T.; Gordon, M. J.; Speck, J. S.; Nakamura, S.; DenBaars, S. P. Wavelength- and size-dependent microLED efficiency gain due to reduced surface recombination and enhanced light extraction. **2023**, No. *Preparing Manuscript*.

**Conference Papers, Presentations, Posters and Talks**

(1) **Smith J.M.** Top-down Fabrication and Testing of microLEDs down to 1μm. Presentation presented at: SSLEEC Review; 2019 Nov; Unversity of California, Santa Barbara.

(2) **Smith J.M.**, DenBaars S.P. FDTD Modeling of Light Extraction in Realistic Flip-Chip InGaN microLEDs. In: Poster Presentation: 13th International Conference on Nitride Semiconductors (ICNS). 2019.

(3) **Smith J.M.** Simulating microLEDs using FDTD. Talk presented at: MOCVD Meeting; 2020 May 5; University of California, Santa Barbara.

(4) **Smith J.M.** Optical Testing of microLEDs. Talk presented at: MOCVD Meeting; 2021 Feb 3; University of California, Santa Barbara.

(5) **Smith J.M.** Size-Dependent Phenomena in μLEDs down to 1μm in diameter. SSLEEC Review; 2021 Nov; Unversity of California, Santa Barbara.

(6) Denbaars S., Wong M., Li P., Li H., **Smith J. M.**, White R., et al. III-nitride-based RGB microLEDs for AR/VR applications. In: Light-Emitting Devices, Materials, and Applications XXVI [Internet]. SPIE; 2022 [cited 2023 Jan 10]. p. PC1202201.

(7) **Smith J.M.** Emerging Challenges and Considerations When Characterizing μLEDs. Presentation presented at: Nitrides Seminar; 2022 May 31; University of California, Santa Barbara.

(8) **Smith J.M.** Size Trends in RGB III-Nitride microLEDs Down to 1μm Diameter. SSLEEC Review; 2022 Nov; Unversity of California, Santa Barbara.

(9) Mohtashami Y., Heki L.K., Wong M.S., **Smith J.M.**, Ewing J.J., Mitchell W.J., et al. Metasurface Light-Emitting Diodes with Directional and Focused Emission. In San Jose, California: Optical Society of America; 2023.

**Patents**

(1) **Smith J.M.**, DenBaars S.P. Formation of microled mesa structures with atomic layer deposition passivated sidewalls, a self-aligned dielectric via to the top electrical contact, and a plasma-damage-free top contact. Unversity of California, Santa Barbara; Application US US17772715 WIPO WO2021086935, 2019. Available from: patentscope.wipo.int/search/en/detail.jsf?docId=WO2021086935

(2) Wong M.S., **Smith J.M.**, DenBaars S.P. Method to improve the performance of gallium-containing light-emitting devices. University of California, Santa Barbara; Application WIPO WO2021086935, 2019. Available from: https://patentscope.wipo.int/search/en/detail.jsf?docId=WO2021087274

ABSTRACT

# III-nitride microLEDs down to 1-micron diameter

by

Jordan M. Smith

Micro-light-emitting diode (microLED, micro-LED, μLED) is an emerging display technology based upon high-density arrays of micron-sized III-nitride (or III-V) LEDs. Small form factor displays, including wearables (smartwatches) and AR (augmented reality) glasses will benefit most from microLED. The paradigm shift from LEDs for solid-state lighting to microLEDs for displays introduces new research challenges. MicroLEDs become difficult to process as dimensions reduce. Mesa diameters as small as 1μm are desirable for maximum resolution and small sizes in AR displays. However, layer-to-layer alignment errors during lithography prevented researchers from fabricating microLEDs below 5μm when using standard LED processing approaches. This thesis presents a self-aligned processing technique developed to circumvent these issues. The result is the smallest microLED ever published at 1μm diameter. This milestone enables new microLED device research at the size ranges most targeted for AR displays. Due to the different usage and requirements for microLEDs in displays

versus LEDs in lighting, new measurement systems for characterizing device performance were constructed. Key considerations when characterizing on-chip microLED electroluminescence are discussed. As dimensions are reduced in microLEDs, new size-dependent physical effects appear. It is well known that microLED efficiency decreases as the diameter shrinks due to increased non-radiative surface recombination. However, results comparing red, green, and blue microLEDs show increasing the indium fraction in InGaN limits surface recombination through enhanced carrier localization. An added effect in small microLEDs is improved extraction efficiency from sidewall reflections redirecting photons within the extraction window. To separate competing size-dependent contributions from sidewall recombination and sidewall reflections, optical models are necessary. A combined approach uses FDTD to model interactions with near-wavelength-sized patterned sapphire features beneath the mesa.

# Contents

1 Introduction ..... 1
1.1 RGB Displays ..... 1
1.2 Comparing display formats ..... 4
1.3 microLED size requirements ..... 7
1.4 Synopsis ..... 9
2 microLEDs for AR ..... 11
2.1 Brightness requirements in augmented reality ..... 11
2.2 Photometric conversions ..... 15
2.3 High nit microLED output ..... 18
3 microLED physics ..... 24
3.1 Quantum Efficiency ..... 24
3.2 Extraction efficiency ..... 27
3.3 Sidewall recombination theory ..... 28
3.3.1 Surface states on III-nitride microLED sidewalls 30
4 Self-aligned microLED fabrication process ..... 32
4.1 Opening the p-via ..... 32
4.1.1 Dry etching 32
4.1.2 Wet etching and other alternatives 34
4.2 Other design goals and considerations ..... 36
4.3 The process ..... 37
4.3.1 Chemical selectivity 39
4.3.2 High-density arrays 41
5 Comparison of size-dependent characteristics of blue and green InGaN microLEDs down to 1 micron diameter ..... 42
6 Wavelength- and size-dependent microLED efficiency gain due to reduced surface recombination and enhanced light extraction ..... 54
6.1 Introduction ..... 54
6.1.1 Red InGaN performance 55
6.1.2 AR applications 55
6.1.3 Red alternatives 56
6.1.4 Growth 57
6.2 Experimental design and wavelength variation ..... 58
6.3 Results ..... 61
6.3.1 Electrical characteristics 61

6.3.2 Efficiency 63
6.3.3 FDTD simulations 65
7 Conclusions ..... 70
8 References ..... 72

# 1

# Introduction

Technologies such as wearable smartwatches and AR (augmented reality) glasses demand displays with more resolution, higher brightness, and lower power consumption than LCD and OLED provide. microLED (or μLED) is a new technology based on micron-sized LED pixels that can supply unprecedented brightness in a small form factor.

## 1.1 RGB Displays

Full-color displays mix red, green, and blue (RGB) subpixels to produce color. The wavelength of light determines the color an observer perceives. Most displays adhere to the Rec. 2020 standard, which defines aspects of the display like resolution (e.g., 4K), aspect ratios, and the wavelengths of the three RGB primaries. Red, green, and blue are 630nm, 532nm, and 467nm, respectively. Figure 1-1 is the 1931 CIE chromaticity diagram with the Rec. 2020 primary wavelengths and sRGB color space overlaid. Most displays operate within the sRGB color space bounded by the white triangle. The outer edge of the colored region (spectral locus) corresponds to monochromatic wavelengths.

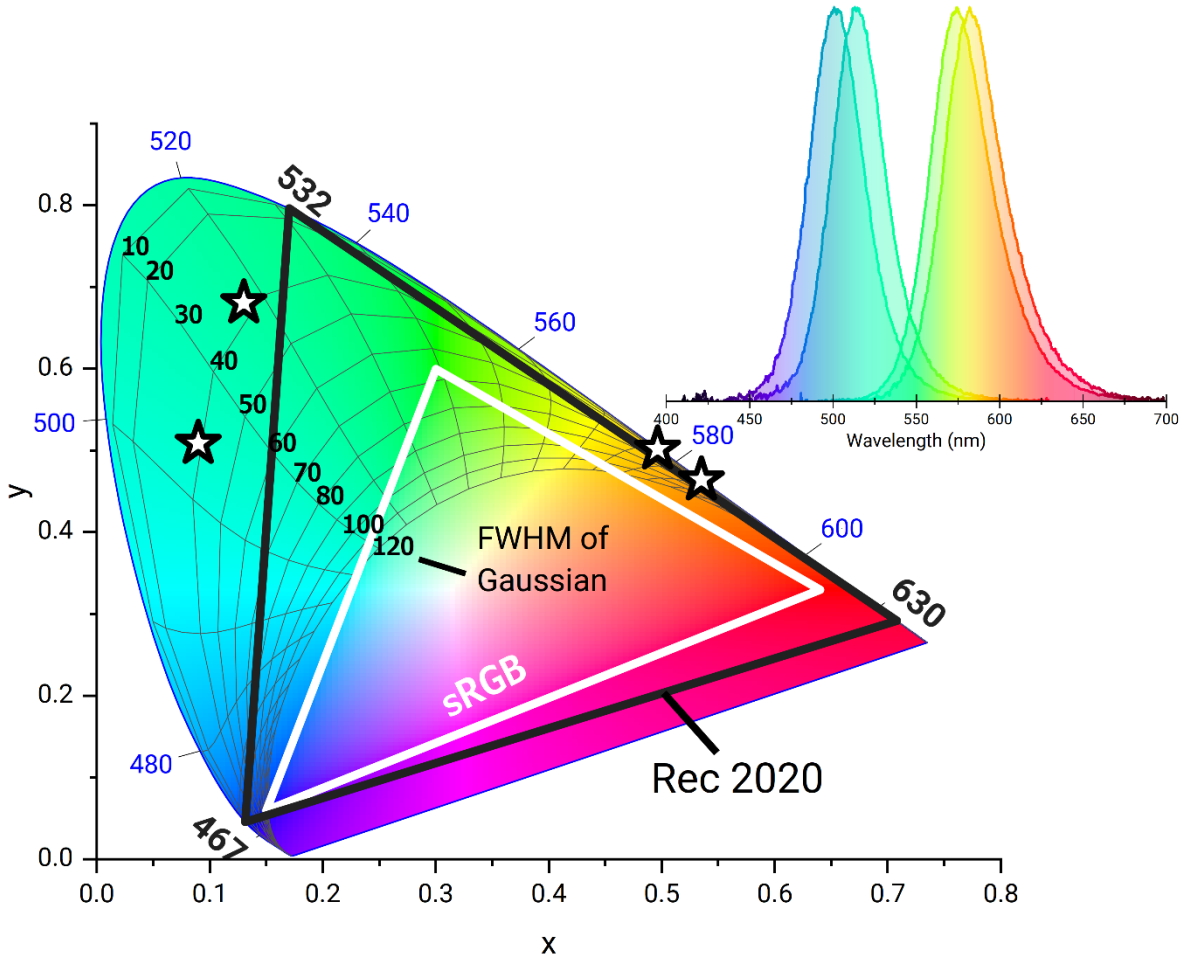



Figure 1-1. CIE 1931 chromaticity diagram overlaid with (white triangle) sRGB color space (black triangle) Rec. 2020 primary wavelengths (stars) xy chromaticity coordinates calculated from the 1µm microLED spectra inlaid in the top right.

In practice, light sources in displays emit a finite range of wavelengths. As the spread increases, the perceived color moves towards the white center of the chromaticity diagram. To illustrate this, the spectra from four 1µm microLEDs are inset in the top right of Figure 1-1. The corresponding xy chromaticity coordinates are overlaid as stars on the diagram. Since they are outside the sRGB color space (white triangle), most monitors cannot accurately represent them.

Spectral spread is commonly quantified as the full-width at half-maximum (FWHM). The black lines webbing Figure 1-1 are produced by varying the FWHM or the center wavelength of an ideal Gaussian spectrum. The stars in Figure 1-1 indicate the FWHM of devices is roughly 40 nm. The devices in Figure 1-1 were all fabricated on one sample diced from a single wafer, which is the subject of section 6.

OLED and InGaN alloys are unique material systems that can actively emit colors across the visible spectrum. InGaN is the only (known) capable semiconductor system, as illustrated in Figure 1-2. However, efficient blue InGaN LEDs only became available in 1993 [1]. The arrival of an efficient blue and white light source also enabled LCD to rise to the top of the display industry, effectively ending the long reign of cathode-ray tube (CRT) displays.

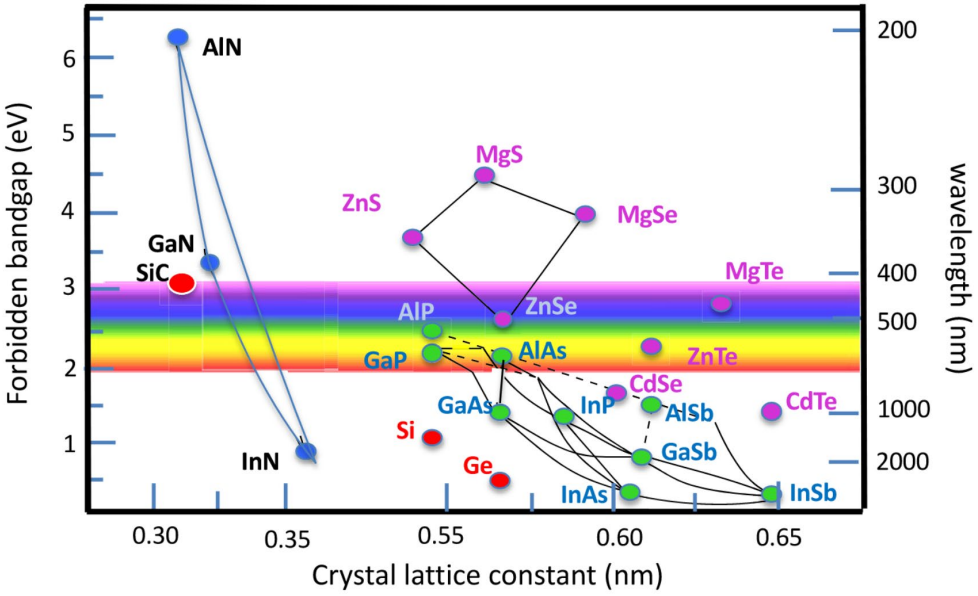


Figure 1-2. Bandgap of major semiconductors. From [2]. CC-BY 4.0.

## 1.2 Comparing display formats

Figure 1-3 illustrates today's standard display formats (excluding projection-based displays such as laser TVs). Figure 1-3a shows direct-view displays, including OLED and microLED (without quantum dot converters). Figure 1-3b shows passive color conversion technology, where blue light or white is down-converted (usually to red and sometimes green). Figure 1-3c illustrates how LCD can filter out other wavelengths of light to produce color.

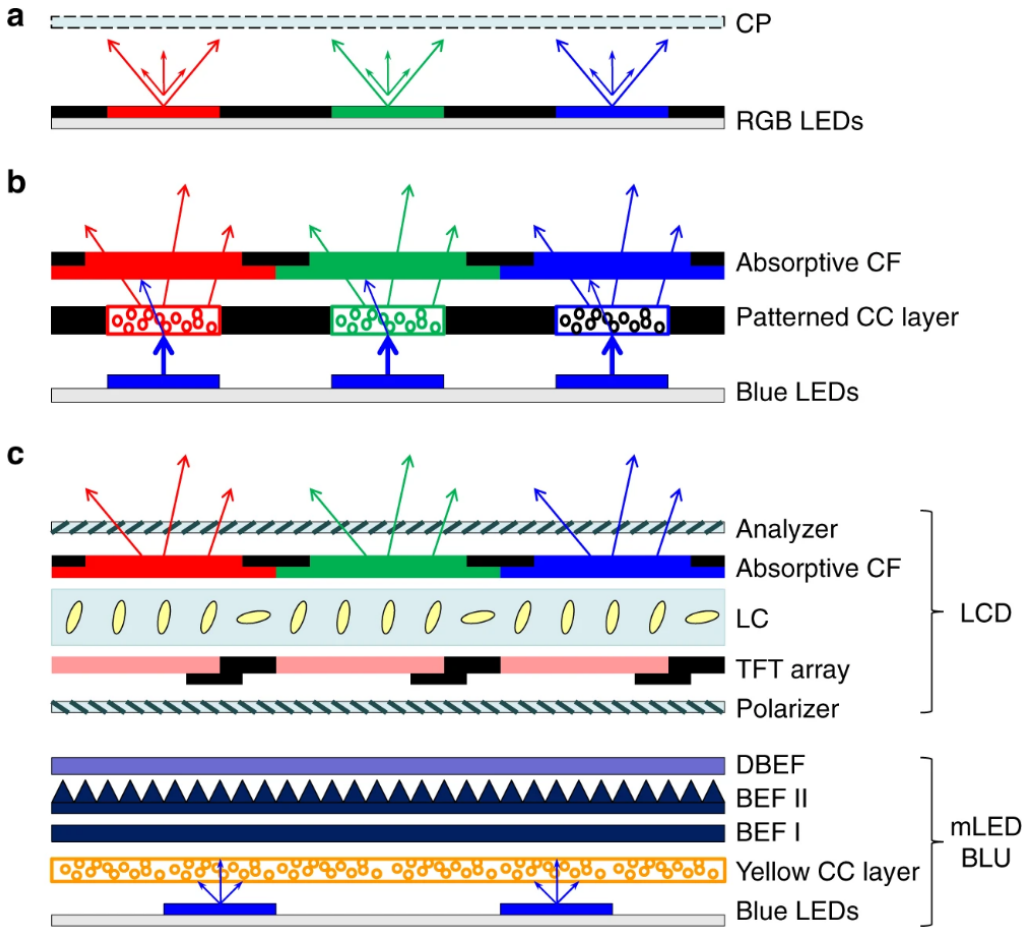



Figure 1-3. (a) Direct-view display representative of OLED and microLED displays. (b) Passive color conversion display. (c) Active color conversion (backlit) displays representative of LCD technology. From [3]. CC-BY 4.0.

Table 1 compares the relative performance metrics of LCD, OLED, and microLED technologies. Based on performance (neglecting cost), microLED can match or outperform OLED and LCD in every category listed. However, the usefulness is strongly dependent on the application.

Table 1. Performance comparison of microLEDs with LCD and organic light-emitting OLED. Adapted from [4]. CC-BY 4.0.

| | LCD | OLED | microLED |
|---|---|---|---|
| Luminous mode | Backlit | Self-luminous | Self-luminous |
| Luminous efficiency | Low | Medium | High |
| Brightness (cd/sqm) | Medium | Low | Very High |
| Contrast | Low | High | High |
| Life (hours) | Medium | Low | High |
| Response time | ms | μs | ns |
| Energy consumption | High | Medium | Low |
| Cost | Low | Medium | High |
| Angular spread | Narrow | Near-Lambertian | Near-Lambertian |

For example, consider a TV that remains indoors and connected to a power source. There is no concern for battery life, so efficiency is unimportant. The brightness output from LCD and OLED are already sufficient for comfortable indoor viewing. OLED is also a direct-view display, so the contrast is comparable to microLED. In this case, it is difficult to foresee an economically sound reason to develop microLED.

microLED production costs continue to decrease, but due to the nature of mass transfer, it should not be assumed ever to become cheaper than OLED.

In mobile applications where battery life is a factor, the efficiency of microLED becomes useful. In outdoor applications, the brightness of microLED can make displays viewable in direct sunlight. Smartwatches are an example where brightness and battery life are crucial. It is no coincidence that Apple has invested in microLED technology, and many expect the Apple Watch to be the first mass-produced microLED display to hit the market.

Eric H. Virey from Yole Group (or Yole Intelligence/Developpement) states (2022) [5],

> "Progress in mass transfer over the last 5 years has been spectacular, to the point that, as of early 2022, most industry players no longer see it as a fundamental roadblock for μLED",

but also concedes (2023) [6],

> "...even in the long term, we struggle to model a cost scenario where microLED would be significantly cheaper than OLED, let alone LCD. Strong performance differentiation against incumbent technologies is therefore required for success in most applications."

Looking back at Table 1, the brightness (per unit area) is the most drastic performance gap when comparing microLED to OLED or LCD. This is the most compelling reason microLED will be the light-engine that powers future augmented reality displays. Section 2 will look specifically at the brightness requirements for AR and prove how microLED may be uniquely capable of fulfilling those requirements.

## 1.3 microLED size requirements

The lateral width range of microLEDs is often cited as 1–100 μm; however, most consumer displays require 1–10 μm. MicroLED widths in contemporary displays are primarily dictated by material cost. Industry groups consistently estimate microLED widths based on allowable manufacturing costs for smartphones (TVs): 3 μm (5–10 μm), Yole Group [6]–[9]; 3 μm (9 μm), Veeco and IHS Research [10]; 4 μm, Intel [11]; and under 5 μm (10 μm), VueReal [12], [13]. Another study found widths for optimal power consumption to be 6, 8, and 16 μm for smartphones, laptops, and TVs [14].

To my knowledge, no peer-reviewed studies warrant microLED pixels over 20 μm in displays. Above 20 μm, there may be applications in backlighting, where devices are usually differentiated as *miniLEDs*. This is limited to displays; there may be alternative applications for microLED, such as communications and optogenetics, which utilize devices above 20 μm.

Perhaps the most significantly researched area in the microLED field is size-dependent efficiency droop that results from increased nonradiative surface recombination as dimensions shrink [15]–[44]. Considering that small size is part of the attraction, there was apparent cause for concern. However, before 2020 [31], there was hardly any efficiency data at dimensions below 5 μm and nothing at 1 μm. This was especially surprising since most microLED displays will need to fall under this range if commercialization is to occur. Figure 1-4 shows a size-dependent peak external

quantum efficiency (EQE) curve commonly seen throughout the literature; however, before 2020 (and even now), the data tended to stop above 5 μm.

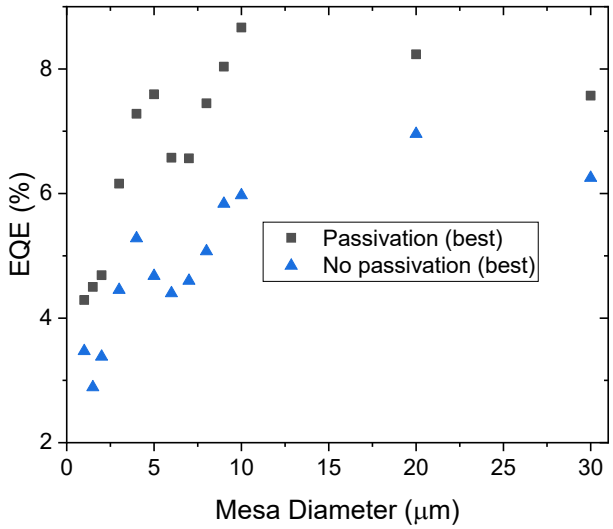



Figure 1-4. Unpublished data comparing blue microLED devices with and without KOH sidewall treatment.

## 1.4 Synopsis

Despite the evidence that almost all displays require 1–10 μm microLED widths, most studies analyze widths above 10 μm and select few approach 1μm [31], [45]–[47]. Limiting the discussion to top-down processing (lithography and etching), this discrepancy is attributed to fabrication equipment limitations, particularly in academic research settings. A self-aligned top-down fabrication technique was developed to address the absence of data at microLED widths necessary for display commercialization. The process enables fabrication of microLEDs down to 1μm diameter, and can be achieved with basic contact alignment, with only three total lithography steps. The process is detailed in Section 4.

Due to the focus on relatively large microLEDs, at least *two additional size-dependent effects* in InGaN microLEDs remain understudied:

1. Extraction efficiency increases as microLED width decreases [26], [32], [48], [49]
2. Surface recombination is reduced as indium content increases [31], [46]

First investigations of microLEDs down to 1μm revealed differences in the size-dependent behavior of blue and green microLEDs; compared to blue, green microLEDs showed mitigated size-dependent EQE droop due to carrier localization around indium-rich regions [31]. Since it is established that surface recombination velocity (SRV) decreases opposite the indium fraction [25], [50]–[53], the findings implied red InGaN microLEDs should further resist size-dependent EQE droop (compared to blue or green InGaN, or red AlInGaP). These results were first published in [31], which is

currently the most cited (non-review) publication containing the term *microLED* or derivatives (i.e., *μLED, micro-LED,* etc). The results are detailed in Section 5.

Recent results confirm that size-dependent droop from surface recombination is further mitigated when moving from green to red. Remarkably, the combination of reduced sidewall effects and increased extraction efficiency is shown to reverse the EQE trend, resulting in size-dependent efficiency *gain* in high indium content microLEDs. These results are detailed in Section 6.

Before the **main research findings in Section 5 and Section 6:**

- Demonstrating why microLED is uniquely suitable for AR in Section 2.
- Physics required for understanding microLED efficiency trends in Section 3.
- microLED fabrication process in Section 4.

# 2

# microLEDs for AR

Due to superior performance (brightness, resolution, efficiency) compared to OLED and LCD—described in the previous section—microLED is considered by many to be the best light engine for AR (augmented reality) displays. AR displays have stricter requirements regarding power, color purity (or wavelength spread), directionality, and resolution. All of these subjects are at the core of the research presented in the following sections, so a review of the optics of AR displays is appropriate.

## 2.1 Brightness requirements in augmented reality

First, an understanding of the end goal for AR glasses for consumers. If AR glasses are to be widely accepted by society, they need to reach the point of being indistinguishable from a standard pair of glasses to a passerby. Until this occurs, AR will not become a pervasive technology. End-user experience directs the overall design [54].

Imagine a pair of glasses. The temple region is the largest area you could feasibly hide a microdisplay system. Depending on the glasses, this region is half an inch wide, or less; however, this means the microLED display must be significantly smaller [55]–[58].

Figure 2-1 depicts a waveguide-based optical combiner, which most experts agree is currently the best solution for achieving the smallest form factor possible, while still meeting the other requirements for a high-quality display.

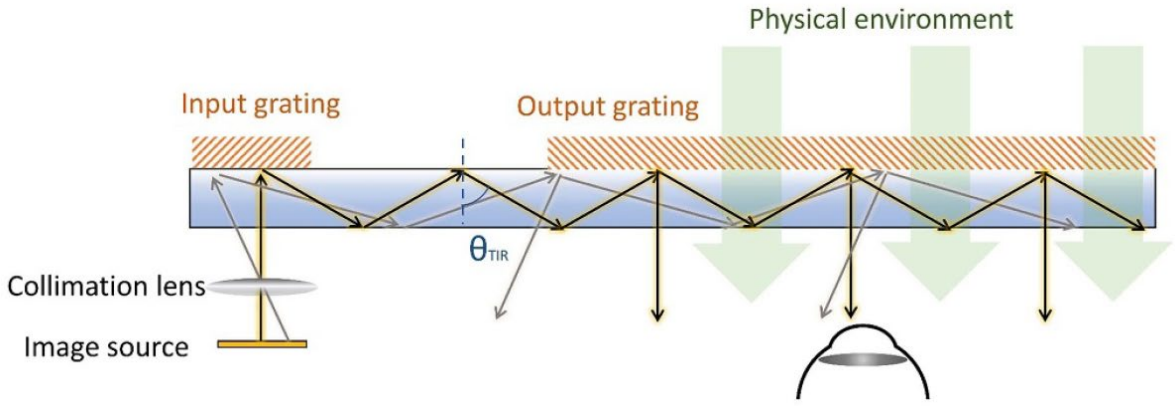



Figure 2-1. A basic structure of a holographic planar waveguide of the eyewear display. From [59]. CC-BY 4.0.

The standard observer's angular resolution limit, or visual acuity, is 60 pixels per degree (PPD). The angular field of view (FoV) limit is over 200 degrees, which is unrealistic for AR currently. FoV is emphasized more in virtual reality (VR) applications. Most AR designs now target under 60 degrees FoV. Eyebox size defines the region of space within the glasses that the observer will be able to see the virtual image. Typically, a lateral eyebox size of 20+ mm is desirable [54], [60]–[62]. These are interdependent on the total number of pixels in the display. If one is increased while the pixel count is constant, another must decrease.

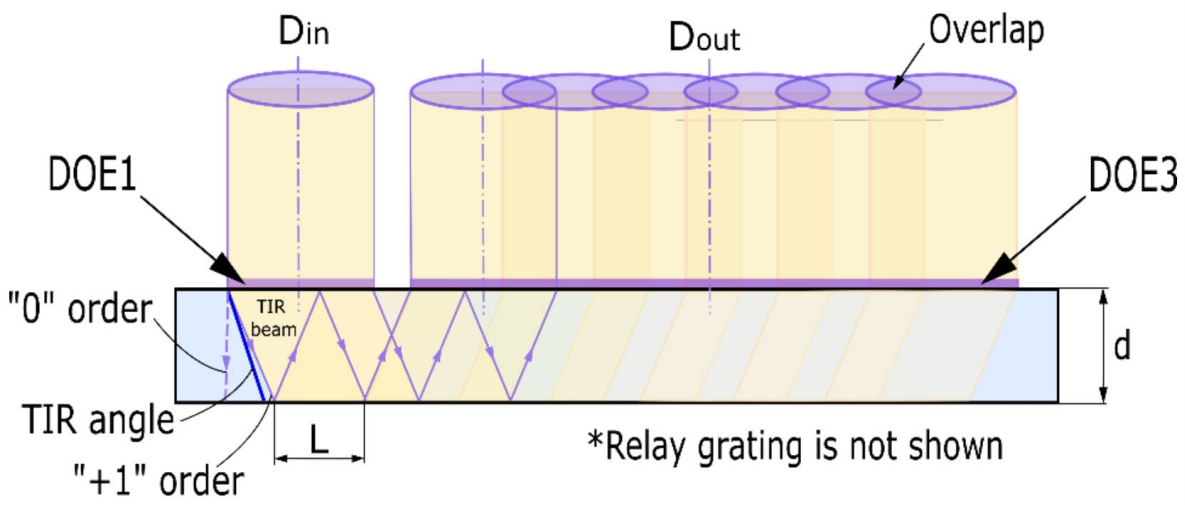



Figure 2-2. Geometry and ray propagation in the substrate: $D_{in}$ is the diameter of the entrance pupil of the substrate, $D_{out}$ is the diameter of the exit pupil of the substrate, L is the beam stoke length. Reproduced from [63]. CC-BY 4.0.

One of the critical features of waveguides is exit pupil expansion (EPE), shown in Figure 2-2. This effect is achieved through diffractive optical elements. When the image is guided down the waveguide, it is replicated multiple times and directed through the exit pupil by a diffractive output coupler. This process of replicating the image is how a large eyebox is achieved. Alternative ways of EPE are available to non-waveguide solutions, although a critical difference is depicted in Figure 2-3. In most other non-waveguide architectures, eyebox expansion requires increasing the thickness of the optics. However, in waveguides, eyebox expansion is achieved solely by increasing the width of the waveguide. Since the waveguide is located within the glasses' lens and (mostly) invisible to the wearer, the increase in width is not a significant concern [59].

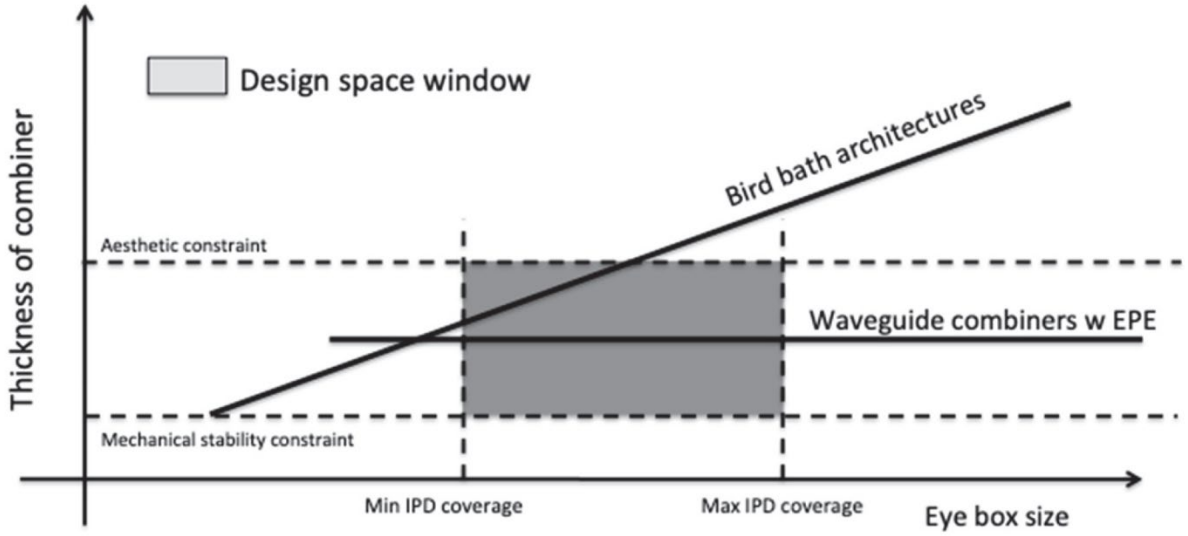



Figure 2-3. The design window addresses both IPD coverage and combiner thickness. Reproduced from [64] with permission from SPIE.

Inevitably, there is a tradeoff. Replicating the image along the waveguide spreads the total number of photons over a larger area. The optical efficiency of waveguides is orders of magnitude lower than alternative designs. Accounting for all the losses, the total efficiency of waveguide systems is 0.1%–1%, while birdbath architectures (in Figure 2-3) is around 10% [65], [66].

Knowing the optical efficiency that can be expected, the required brightness output from the display can be determined if the maximum brightness that must be delivered to the observer is known. In bright outdoor conditions, several thousand nits from the sun can be expected. The sun sets the target brightness at roughly 10,000 nits *at the eye* to see an image on a bright day. If the efficiency is 1%, the display must

produce 1,000,000 nits (1 Mnit or 1 Mcd/m$^2$) to account for losses. At 0.1% efficiency, an astounding 10,000,000 nits.

Although far from an expert on LCoS/LCD or OLED, I have not found a source claiming anything approaching 100,000 nits from LCD, while OLED is about an order of magnitude lower than LCD. On the other hand, multiple startup microLED have reported microLED displays capable of producing millions of nits [55]–[57]. These sources are not verified, so the next sections prove that such a goal is certainly possible for microLED.

## 2.2 Photometric conversions

The preceding section showed that AR designers might expect microLED displays to produce at least 1,000,000 nits to compensate for lossy waveguides. These sections aim prove whether 1 Mnits is a realistic expectation. First, a brief review of converting from radiometric to photometric values is necessary.

The measured radiometric quantities must be converted to photometric quantities to calculate nits. Photometric quantities consider how the standard observer perceives the brightness of light at different wavelengths (or colors). The strongest visual response occurs in the green region of the electromagnetic spectrum at a wavelength of 555nm. The left axis of Figure 2-4 shows the CIE 1924 photopic luminosity function, $V(\lambda)$, which quantifies the relative brightness response of the eye at different wavelengths across the visible spectrum. The CIE 1931 color matching

functions were designed such that $\overline{y}(\lambda)$ is equivalent to $V(\lambda)$, although the latter is much more commonly used in this context.

Accurately calculating photometric quantities from radiometric quantities requires knowing the *spectral* radiometric quantity. In the case of microLEDs measured throughout this work, the measurement system is calibrated to measure the spectral flux (or more precisely, spectral radiant flux), $\Phi_{e,\lambda}(\lambda)$, in units of watts per unit wavelength (W/nm). The notation adopted differentiates radiometric and photometric equivalents by the subscript *e* and *v*, for energy and visual, respectively. The second subscript, $\lambda$, indicates it is a spectral quantity. In other words, $\Phi_{e,\lambda} = \frac{\partial \Phi_e}{\partial \lambda}$.

In Eq. 1, integrating the spectral flux over wavelength gives the total optical power in watts (W).

$$\Phi_e = \int_{\lambda_{min}}^{\lambda_{max}} \Phi_{e,\lambda}(\lambda)\ d\lambda, \qquad \text{Eq. 1}$$

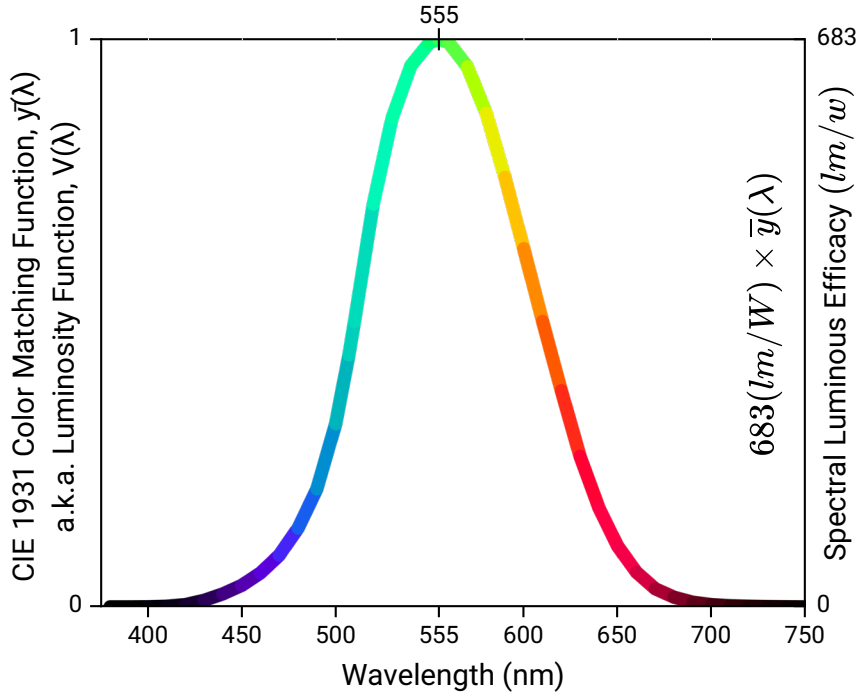



Figure 2-4. (left axis) CIE 1924 photopic luminosity function, denoted $V(\lambda)$, which is equivalent to the CIE 1931 color-matching function, denoted $\overline{y}(\lambda)$. (right axis) Represents the lumens per watt perceived at the corresponding wavelength. At peak efficiency, 1 W of 555 nm monochromatic light would have a perceived brightness of 683 lm. $K_m$ is a scaling constant defined as 683 lm/W.

Eq. 2 is a ubiquitous formula for converting from a radiometric quantity to its photometric counterpart by substituting $\Phi_{e,\lambda}(\lambda)$. In practice, it is simpler to absorb the scaling factor of 683 (lm/W) into the luminosity function $\overline{y}(\lambda)$, resulting in the right axis of Figure 2-4. This is sometimes referred to as the spectral luminous efficacy.

$$\Phi_v = 683.002\ (lm/W) \cdot \int_{\lambda_{min}}^{\lambda_{max}} \overline{y}(\lambda)\Phi_{e,\lambda}(\lambda)\ d\lambda \qquad \text{Eq. 2}$$

Prior to integrating, Eq. 2 can be further simplified by taking the product of the experimentally measured (radiometric) spectral radiant flux (W/nm) and the spectral

luminous efficacy (lm/W) to get the photometric equivalent, the spectral luminous flux (lm/W), $\Phi_{v,\lambda}(\lambda)$:

$$\Phi_V = \int_{\lambda_{min}}^{\lambda_{max}} \Phi_{v,\lambda}(\lambda)\ d\lambda. \qquad \text{Eq. 3}$$

## 2.3 High nit microLED output

A green and violet 1μm microLED were chosen for comparison, since the calculation of nits high strongly dependent on the wavelength (Figure 2-4). The violet microLED is significantly more efficient at the peak EQE, but green light elicits a much stronger response. The measured output from the two devices is plotted in the top row of Figure 2-5. However, the devices have similar efficiencies at the operating current densities chosen, shown above each figure.

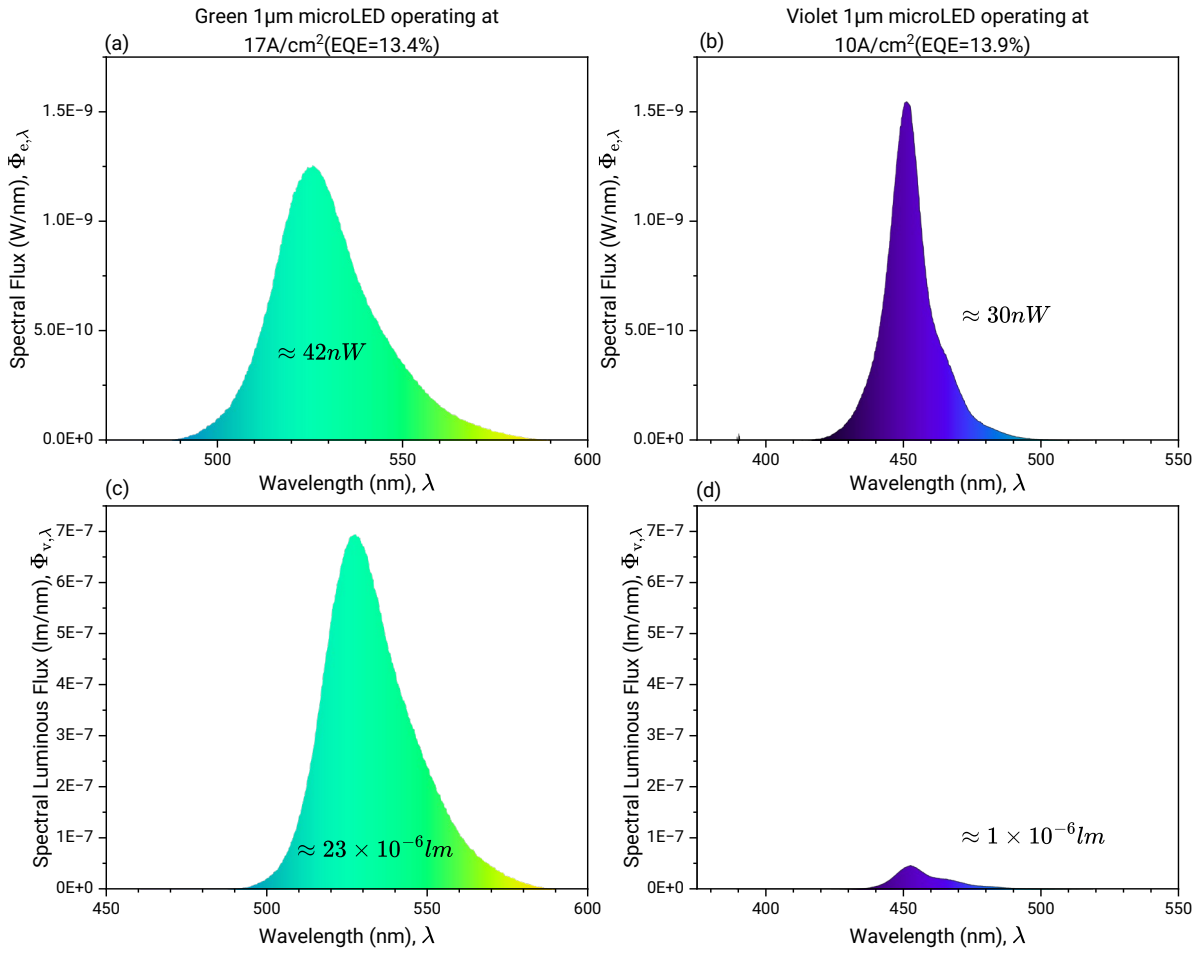



Figure 2-5. Comparison of measured radiometric (top) spectra and the calculated photometric (bottom) counterparts for green (left) and violet (right) 1μm diameter microLEDs. (top row) Spectral flux obtained from electroluminescence measurements using a radiometrically calibrated integrating sphere in 2π steradian collection angle configuration. (bottom row) Spectral luminous flux calculated from the product of the top row spectra and the spectral luminous efficacy function (right axis of Figure 2-4). Corresponding numerically integrated values displayed with each spectrum.

The bottom spectra are obtained by multiplying the spectra in the top row with the right axis of Figure 2-4 (the spectral luminous efficacy). Since the visual response is lower in the violet region, the photometric spectra in the bottom right of Figure 2-5 is significantly reduced relative to the green device. The integrated spectra in nanowatts and lumens are listed in the top and bottom panels, respectively.

In order to calculate the nits from the integrated spectra in the bottom of Figure 2-5, we must divide by the solid angle and also divide by the area occupied by 1 pixel. Unfortunately, bonding high density arrays of microLEDs is beyond our capabilities. However, the process used to fabricate the microLEDs is capable of producing high density arrays of 1μm devices with high yield. Figure 2-6 shows 1μm microLEDs arrayed in a hexagonal packing arrangement, where the distance between nearest neighbors is 2μm.

Assuming the pixel density in Figure 2-6 and a solid collection angle of 2π sr (taken from the integrating sphere measurement geometry), the nits can be calculated. Figure 2-7 plots the resulting luminance and nits as the current density is swept. At each current density, spectra like those in Figure 2-5 are acquired. The EQE and centroid wavelength are also plotted versus current density, corresponding to the left axes.

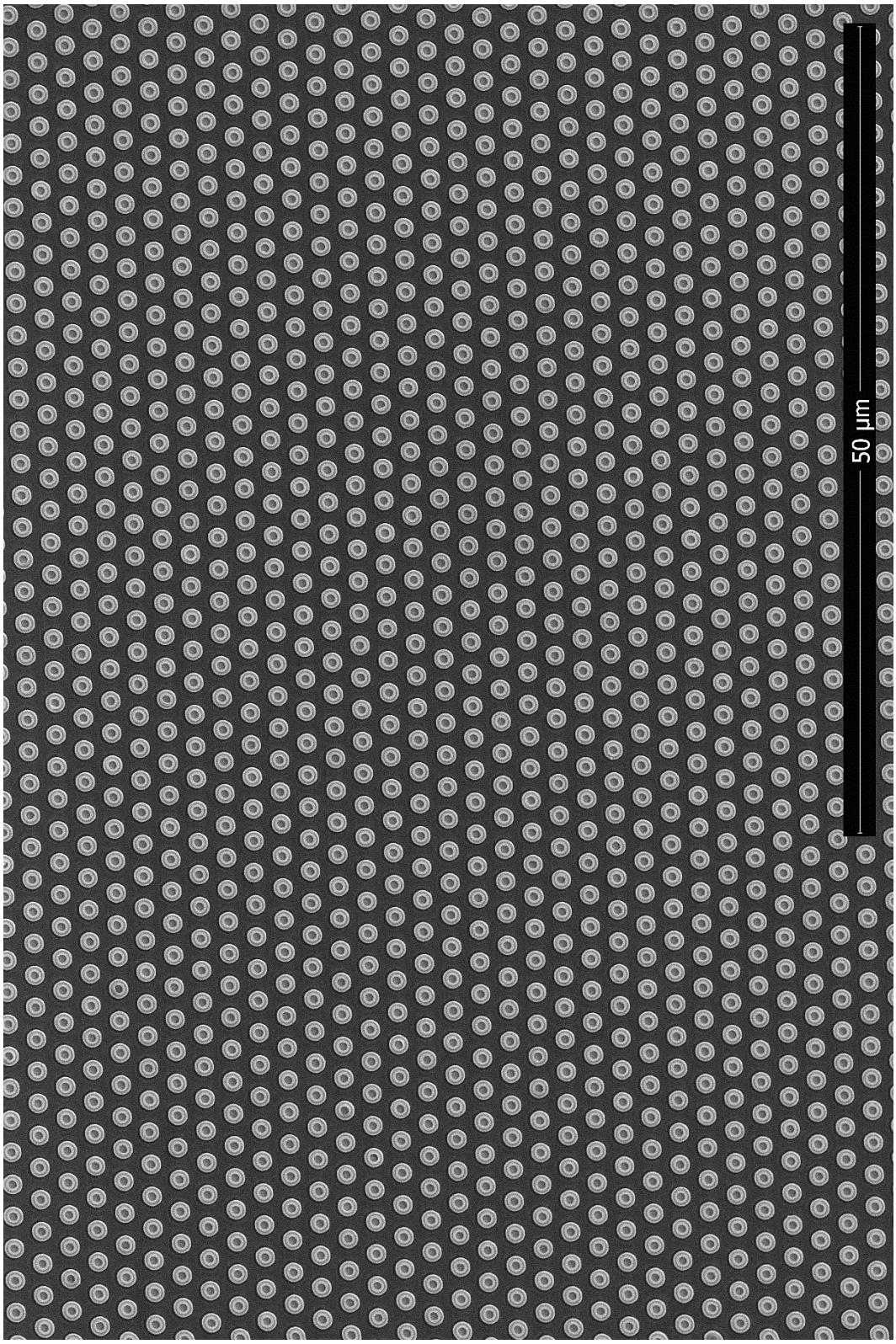



Figure 2-6. 1µm microLED mesas arrayed in a 2D hexagonal packing arrangement with 2µm nearest neighbor pitch. 2D hexagonal packing is 15.4% more dense than square packing.

The nits on the right axes of Figure 2-7 show both 1μm microLEDs are indeed capable of producing millions of nits. The enlarged dots on the curves in Figure 2-7 indicate the slice at which the spectra shown in Figure 2-5 were measured. The top panels are replotted in the bottom right corner of Figure 2-7 to compare the green and violet devices.

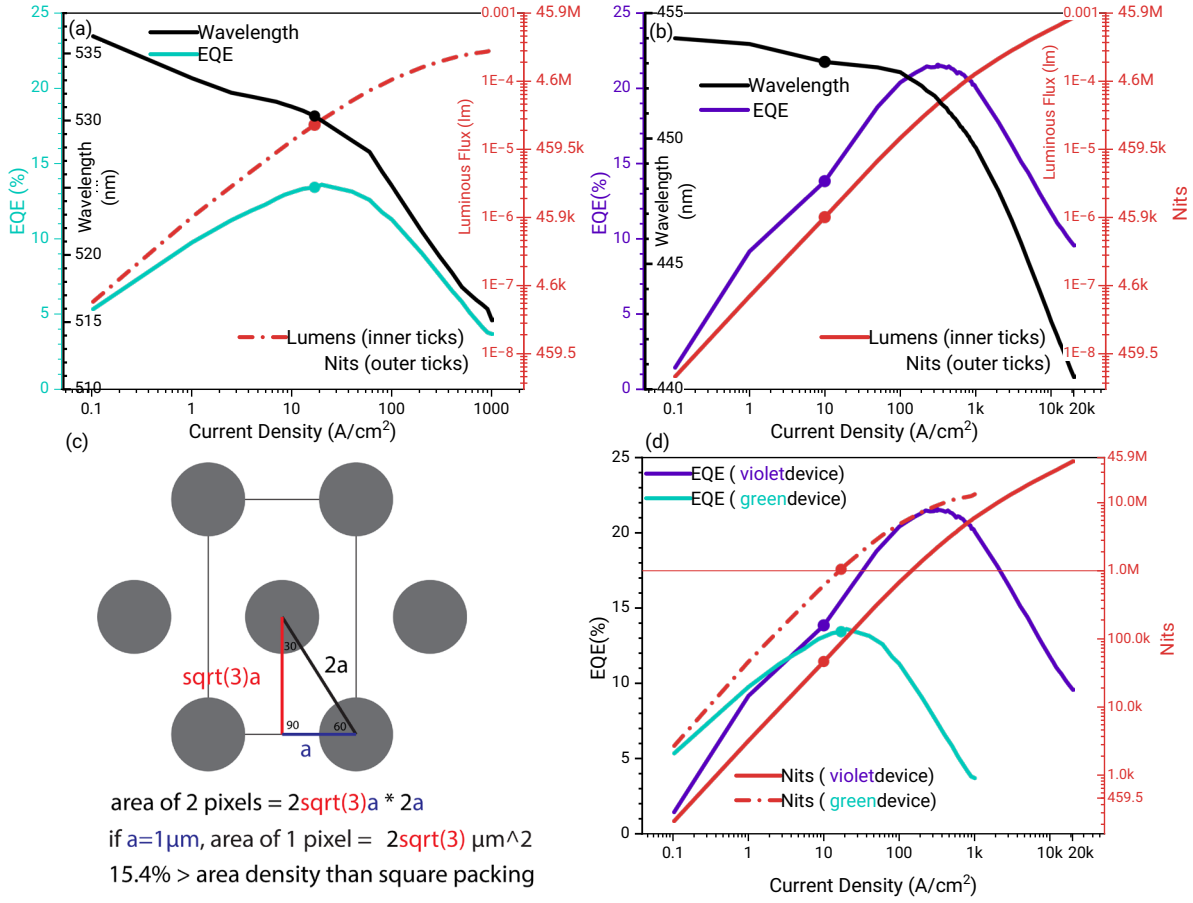



Figure 2-7. (a) Green and (b) violet plot the EQE (outer left axis), centroid wavelength (inner left axis), and luminous flux/Nits on the inner/outer right axis as a function of current density for the same green 1μm device in Figure 2-5. (d) Replots the EQE and nits axes from (a) and (b) on the same scale, and marks the 1 million nits threshold. (c) shows the assumption made for calculating the area of a pixel in order to convert from lumens to nits, based off the demonstrated high density array shown in Figure 2-6. Collection solid angle for conversion to nits is 2π sr.

Although the EQE of the green device is lower than the violet, it outputs higher nits than the violet device at any current density. The bottom right of Figure 2-7 shows the 1 million nit threshold, which can be seen to intersect the nits curve for the green device very near the point where the spectra shown in Figure 2-5 was taken.

1μm green device summary:

- At *1 Mnit* threshold:
  - $J=17 A/cm^2$
  - *EQE=13.4%*
- At peak EQE:
  - same as 1 Mnit threshold above
- At peak current density:
  - $J=1000 A/cm^2$
  - *EQE=3.5%*
  - *10 Mnits*

1μm violet device summary:

- At *1 Mnit* threshold:
  - $J=100 A/cm^2$
  - *EQE=17.4%*
- At peak EQE:
  - *EQE=22%*
  - $J=200 A/cm^2$
  - 9 Mnits
- At peak current density
  - $J=20000 A/cm^2$
  - *40 Mnits*

# 3

# microLED physics

## 3.1 Quantum Efficiency

The external quantum efficiency (EQE) is the ratio of photons extracted from the device to the number of carriers injected into the active region active region. It is also the product of the internal quantum efficiency $EQE$, the injection efficiency, $INJ$, and the extraction efficiency, $EXT$.

$$EQE = EXT \cdot INJ \cdot IQE = EXT \cdot INJ \cdot \frac{Bn^2}{An + Bn^2 + Cn^3} \quad \text{Eq. 4}$$

From the righthand $IQE$ is the right term:

$$IQE = INJ \cdot \frac{Bn^2}{An + Bn^2 + Cn^3} \quad \text{Eq. 5}$$

This form of the $IQE$ is called the ABC model, where the $ABC$ coefficients are assigned to different recombination pathways that can occur in the active region. The $B$ coefficient describes the radiative recombination desired in LEDs. $C$ is commonly attributed to Auger recombination which is now believed to be the main source of droop in III-nitrides at high current densities. In microLEDs, the $A$ coefficient is of interest as it can be modified slightly to include the effects of surface recombination, which is discussed shortly.

The $IQE$ can also be described without the use of fitting coefficients more simply as the ratio of the radiative recombination rate, $R_r$, to the total sum of radiative and nonradiative ($R_{nr}$) recombination rates:

$$IQE = \frac{R_r}{R_r + R_{nr}} = \left(1 + \frac{\tau_r}{\tau_{nr}}\right)^{-1} \quad \text{Eq. 6}$$

Unlike the internal quantum efficiency, the $EQE$ can be directly measured experimentally. For monochromatic light, the $EQE$ equation takes the form:

$$(monochromatic)\ EQE = \frac{\lambda_{mono} \cdot \Phi_{e,mono}}{J \cdot \mathcal{A} \cdot \frac{hc}{q}}. \quad \text{Eq. 7}$$

For convenience, Eq. 7 is modified for microLED measurements by replacing the current with the current density multiplied by the area of the device, $I = J \cdot \mathcal{A}$. However, the distribution of photons emitted from LEDs occurs over a finite range of wavelengths; to account for this, the power in Eq. 7 is actually:

$$\Phi_e = \int_{\lambda_{min}}^{\lambda_{max}} \Phi_{e,\lambda}\ d\lambda, \quad \text{Eq. 8}$$

Where the spectral (radiant) flux is $\Phi_{e,\lambda} = \frac{\partial \Phi_e}{\partial \lambda}$.

Returning to Eq. 7, it must be changed to account for the wavelength dependence:

$$EQE = \frac{\int_{\lambda_{min}}^{\lambda_{max}} \lambda \cdot \Phi_{e,\lambda}\ d\lambda}{J \cdot \mathcal{A} \cdot \frac{hc}{q}} \quad \text{Eq. 9}$$

It is now possible to calculate the $EQE$ after acquiring a spectral flux $\Phi_{e,\lambda}$ over the wavelength interval $\lambda_{min}$ to $\lambda_{max}$. The product $\lambda \cdot \Phi_{e,\lambda}$ can then be numerically integrated over the wavelength range in the numerator of Eq. 9.

However, it is of interest to be able to refer to the wavelength of the LED when discussing integrated metrics such as the EQE and optical power (or radiant flux). Often, the peak wavelength of the spectra is used for this purpose. However, a more descriptive definition is the centroid wavelength, $\langle\lambda\rangle$, of the spectra $\Phi_{e,\lambda}$. This is the wavelength at which, on either side, the area (the integral) is equal. In other words, $\langle\lambda\rangle$, is the wavelength at which the following statement is true:

$$\frac{\Phi_e}{2} = \int_{\lambda_{min}}^{\langle\lambda\rangle} \Phi_{e,\lambda}\, d\lambda = \int_{\langle\lambda\rangle}^{\lambda_{max}} \Phi_{e,\lambda}\, d\lambda, \qquad \text{Eq. 10}$$

It can be shown that the centroid wavelength is also equal to the numerator of Eq. 9 divided by the integrated power, Eq. 8, which should appear obvious after inspecting the equation:

$$\langle\lambda\rangle = \frac{1}{\Phi_e} \int_{\lambda_{min}}^{\lambda_{max}} \lambda \cdot \Phi_{e,\lambda}\, d\lambda \qquad \text{Eq. 11}$$

By replacing the monochromatic wavelength and power terms in Eq. 7 with the polychromatic versions (representing a real LED), the EQE can also be calculated:

$$EQE = \frac{\Phi_e \cdot \langle\lambda\rangle}{J \cdot \mathcal{A} \cdot \frac{hc}{q}} \qquad \text{Eq. 12}$$

## 3.2 Extraction efficiency

AR requires smaller pixels approaching 1μm to simultaneously maximize resolution as pixels per degree (PPD), field of view (FoV), and eyebox size while minimizing form factor [62], [67], [68]. Diffractive waveguides are the most popular optical combiners capable of meeting these design requirements relatively cheaply [54]. However, small acceptance angles coupled with broad angular emission from microLEDs (or OLEDs) contribute to system optical efficiencies (from display to eye) under 1% [66], [69], [70]. Poor coupling efficiency can be partially recovered by collimating microLED emission with wafer-level optics, such as microlens arrays [71]–[74].

As it turns out, microLED emission can also be collimated simply by reducing the lateral width. Models [32], [49], [75]–[79] and experiments [26], [32], [48] show that decreasing microLED width induces a self-collimating effect due to light reflecting against tapered sidewalls and redirecting toward the extraction window. In Ley *et al.* [32] we demonstrated external quantum efficiency (EQE) of KOH-treated blue microLEDs rose from 8.5–13.5% as diameter decreased from 20–2μm due to enhanced light extraction, as shown in Figure 3-1.

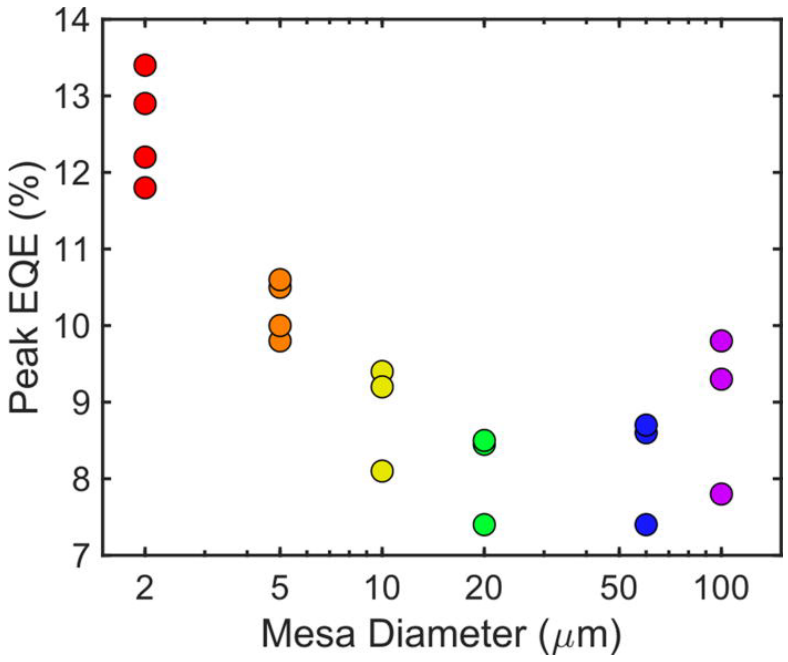



Figure 3-1. Peak EQE versus blue microLED diameter. Reproduced from [32] with the permission of AIP Publishing.

## 3.3 Sidewall recombination theory

In order to predict which surface passivation treatments may be most effective, it is first necessary to understand the origins of surface recombination. We start by defining the surface recombination rate per unit area:

$$R_s = \frac{pn - n_i^2}{p + n + 2n_i \cosh\left(\frac{E_i - E_{st}}{kT}\right)} N_{st} v_{st} \sigma \qquad \text{Eq. 13}$$

Where $p$, $n$, and $n_i$ are the hole, electron and intrinsic carrier concentrations, respectively. $E_i$ is the intrinsic fermi energy and $E_{st}$ is the energy of a surface state

located in the band gap. The final three terms together define the surface recombination velocity:

$$v_s = N_{st} v_{st} \sigma \qquad \text{Eq. 14}$$

$N_{st}$ is the density of surface states at energy $E_{st}$, $v_{st}$ is the thermal velocity of carriers, and $\sigma$ is the capture cross section of the surface state. Experimental recombination velocities for III-V and III-nitride semiconductors are shown in Figure 3-2 [80].

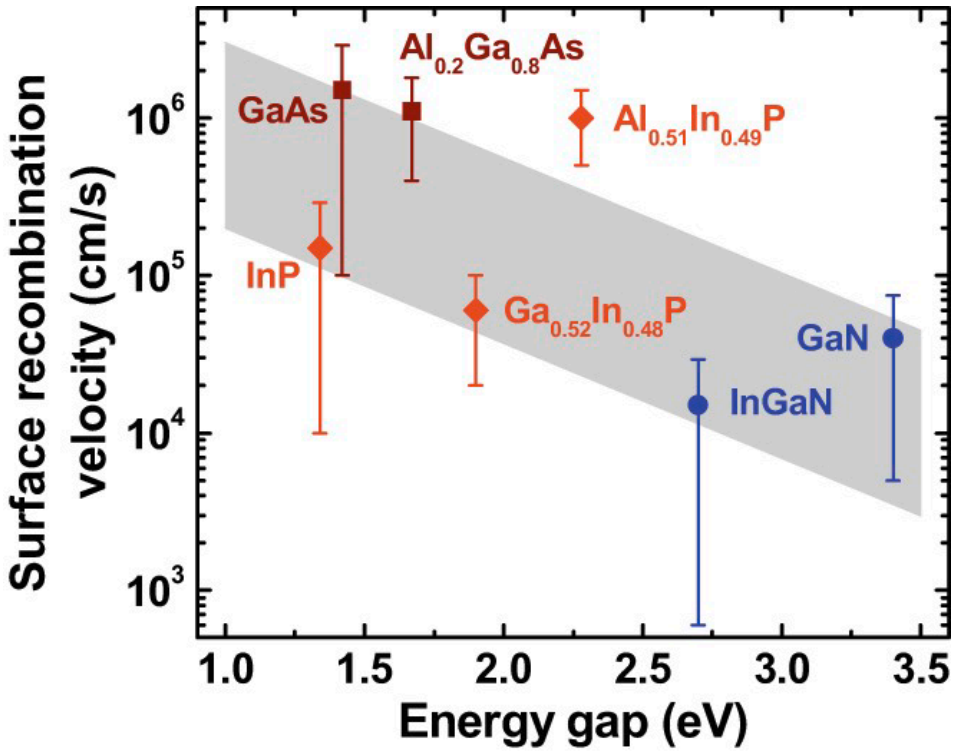



Figure 3-2. Ranges of experimentally measured surface recombination velocities for III-V and III-N alloys compiled from various sources by [80]. Bars show the ranges of the reported values, whereas symbols indicate the most frequent/averaged ones. Grey shadow demonstrates a general trend of the surface recombination velocity variation with the materials bandgap. Reproduced from [80] with permission from Wiley.

The recombination velocity (Eq. 14) can be used to calculate an effective SRH coefficient, $A'$, in the ABC recombination model that is dependent on the perimeter and area of the active region [81]:

$$A' = A_0 + v_s \frac{\mathcal{P}}{\mathcal{A}} \quad \text{Eq. 15}$$

Examining the surface recombination rate shows nonradiative recombination can be reduced by reducing the density of surface states, $N_{st}$. These surface states have several origins, including impurities, surface defects (i.e., nitrogen vacancies in GaN), and dangling bonds. Additionally, the $E_i - E_{st}$ term in Eq. 13 reveals that defects nearer to mid-gap are more effective nonradiative recombination centers. By reducing the number of surface states, $N_{st}$, in the gap, the effective $A'$ coefficient will be reduced [82].

### 3.3.1 Surface states on III-nitride microLED sidewalls

Understanding how the bonding on InGaN surfaces gives rise to defect states in the bandgap is crucial. Unfortunately, various growth and experimental limitations prevent direct study of the surface of InGaN active regions on the sidewall formed by dry etching. We are forced to examine models and experimental results conducted on planar III-nitride surfaces with the expectations they translate (at least partially) to InGaN microLED sidewalls.

#### 3.3.1.1 Intrinsic surface states

Beginning with an ideal semiconductor surface, intrinsic surface states resulting from dangling bonds can be understood from the viewpoint of the tight binding approximation [83]. The reduced bonding of atoms near the surface shifts the energy closer to their unbonded atomic states which exist nearer the bandgap. In semiconductors with ionic nature such as GaN, the cation dangling bonds (Ga), give rise to higher energy acceptor states while the anion (N) gives rise to donor states nearer the valence band. In fact, in GaN it is believed that the energy level of nitrogen-derived dangling bond states are outside the bandgap below the valence band due to the large electronegativity of nitrogen [84], [85].

#### 3.3.1.2 Extrinsic surface states

In addition to intrinsic surface states at the surface of a perfectly terminated crystal, extrinsic surface states originating from crystallographic defects and foreign impurities may also exist and should be avoided. In etched GaN, the crystallographic defects are typically nitrogen vacancies (which explains Ga-rich surfaces after etching). Impurities on GaN surfaces are typically native oxides and carbon [86].

# 4

# Self-aligned microLED fabrication process

## 4.1 Opening the p-via

Layer-to-layer misalignments during lithography steps is the limiting factor when fabricating small microLEDs, particularly in academic settings which lack the proper stepper systems necessary. At UCSB, the best repeatable alignment error that can be achieved is 250nm. When considering fabricating a 1 μm device, this alignment error is unacceptably high. For example, etching a 500nm p-via over a 1μm wide mesa allows no more than 250nm alignment error. To address the absence of data at microLED widths necessary for display commercialization, [31] introduced a self-aligned top-down process to fabricate 1μm microLEDs.

### 4.1.1 Dry etching

Although dry etching the dielectric aperture (or p-via) offers the best control and repeatability, it also introduces size-dependent damage to the p-contact. Since the main objective of many microLED papers is to investigate size-dependent sidewall recombination, this is a significant problem as it becomes difficult to decouple the two phenomena.

Damage from dry-etching occurs because it is challenging, if not impossible, to etch holes of varying diameter at the same rate due to various loading effects. The

result is that microLEDs of varied sizes receive varying degrees of exposure to plasma damage at the p-contact. This effect was observed and corrected by Olivier and Daami [30], [87], and shown in Figure 4-1. A more recent study [88] specifically addresses and confirms this.

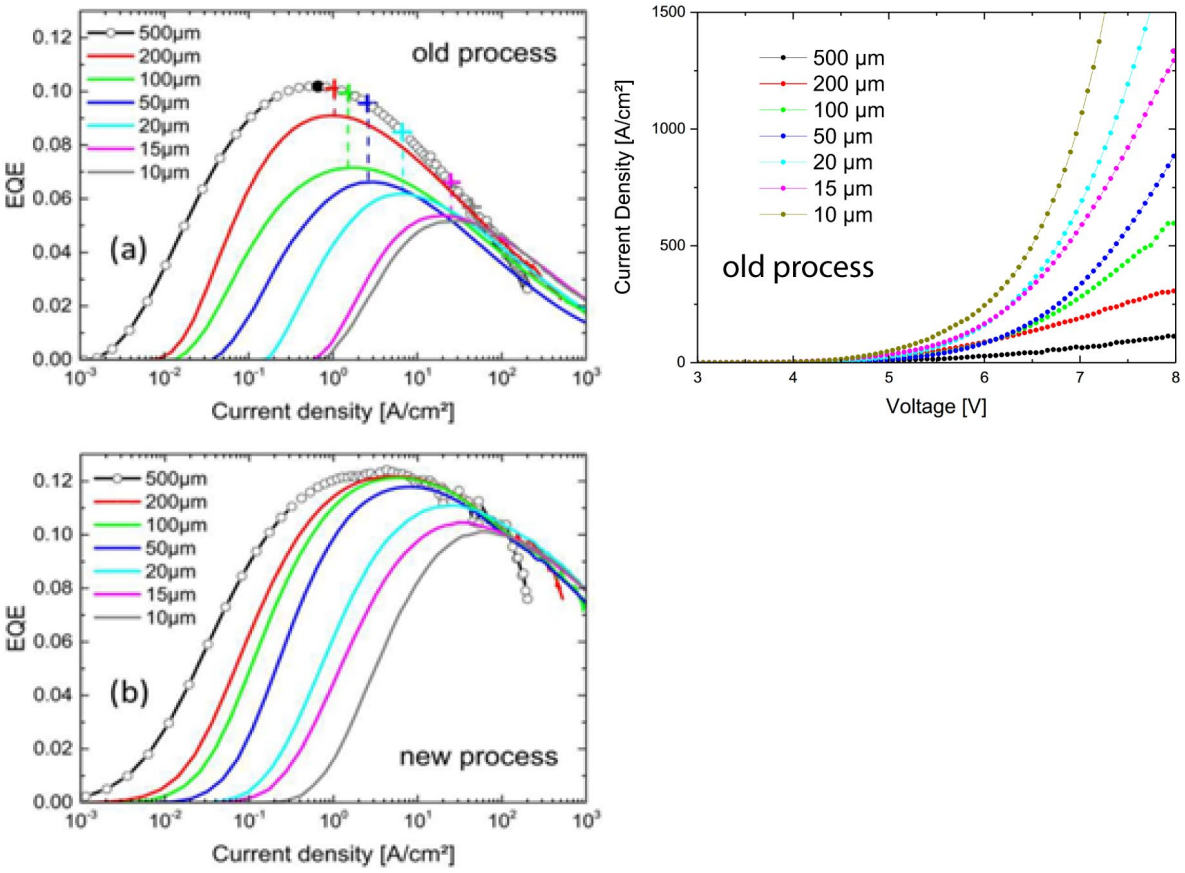



Figure 4-1. (left) EQE comparison of devices fabricated under different plasma etching conditions for the opening of the p-via. (a) Unoptimized and (b) optimized. Specifics of the etch optimization are not provided. (top right) Same devices from unoptimized old etch process in top left. Devices show clear signs of large differences in series resistance versus size. (left) From [30] with permission from Wiley. (right) From [89] with permission from Elsevier.

The deviation between sizes in the IV curves at high current densities shown in Figure 4-1 shows a difference in the series resistance between device sizes. However, leakage current due to sidewall recombination should manifest as a parallel resistance

which dominates at low current densities (seen clearly in Figure 5-3). This represents one of the largest errors commonly seen microLED fabrication in the literature (I estimate over half of the IV curves I see clearly show size-dependent series resistance).

### 4.1.2 Wet etching and other alternatives

Fortunately, at UCSB, all microLED processes avoid directly etching the dielectric aperture (admittedly, without contact damage in mind). The process often employed by D. Hwang, M. Wong, and most others, uses a buffered HF (BHF) etch to open the p-via in $SiO_2$. Figure 4-2 compares plasma-etched p-vias on microLEDs fabricated by Olivier et. al. (the same devices in Figure 4-1) with BHF-etched devices fabricated by D. Hwang [90]. R. Ley used a plasma etch to open the p-via in [32], but also used an $Al_2O_3$ etch-stop to protect the contact.

A final non-damaging alternative is a liftoff process to form the p-via. However, both liftoff and wet etching become intractable when microLED dimensions approach 1μm, due to mentioned alignment errors. Unless, of course, the alignment error is removed completely through a self-aligned approach.

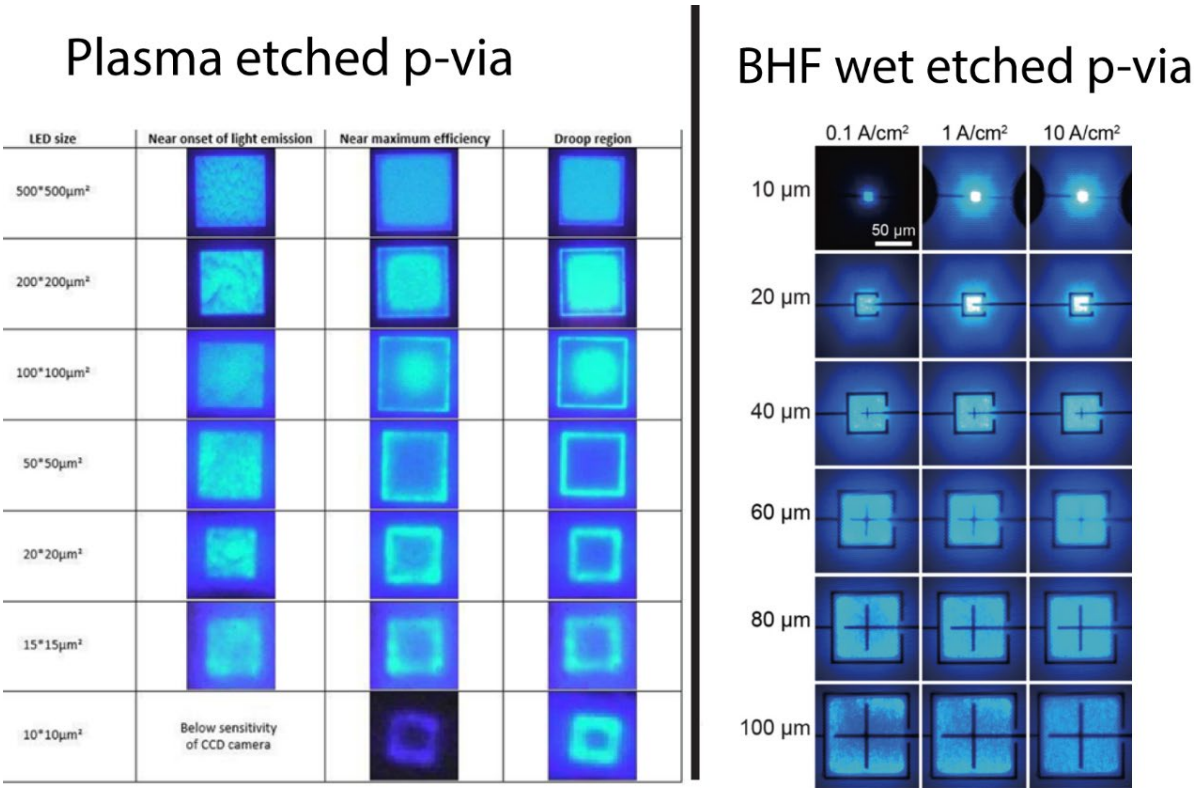



Figure 4-2. Electroluminescence images of microLEDs with (left) plasma dry etched p-vias (corresponding to the same devices in the top row of Figure 4-1). From [89] with permission from Elsevier. (right) BHF wet etched p-vias with uniform light distribution. From [90] with permission from IOP publishing.

## 4.2 Other design goals and considerations

- Enable fabrication of devices down to (at least) 1μm, but also allow for fabrication of larger devices (to study a wide range of sizes)
- Allow for a wide range of wet chemicals for sidewall treatment studies, including both bases and acids (e.g., KOH and Piranha)
- Make the process as quick, simple, and commercially-viable as possible [91]
    - No electron-beam lithography
    - Increase the speed of learning cycles
- Allow for high-temperature processing
    - Tunnel junction activation
    - Atomic layer deposition (ALD)
- Allow for high-density arrays to be fabricated, as opposed to single devices
    - In the event we could integrate the devices in a full display
- Self-aligned ITO p-contact was chosen for several reasons:
    - Silver-based p-contacts are notoriously challenging
    - Self-aligned ITO contact cuts a lithography step by allowing for identical p- and n-pads (Al/Ni/Au), which are nearly as reflective as Ni/Ag
    - If the contact does not cover the entire mesa, and only contacts the part exposed by the p-via, then another size-dependent feature is introduced
        - The degree of effect would presumably change depending on the amount of misalignment of the p-via relative to the mesa

## 4.3 The process

The process is illustrated in Figure 4-3. In only 3 lithography steps (which can be performed with a basic contact aligner) microLEDs with diameters down to 1µm (or smaller) can be fabricated.

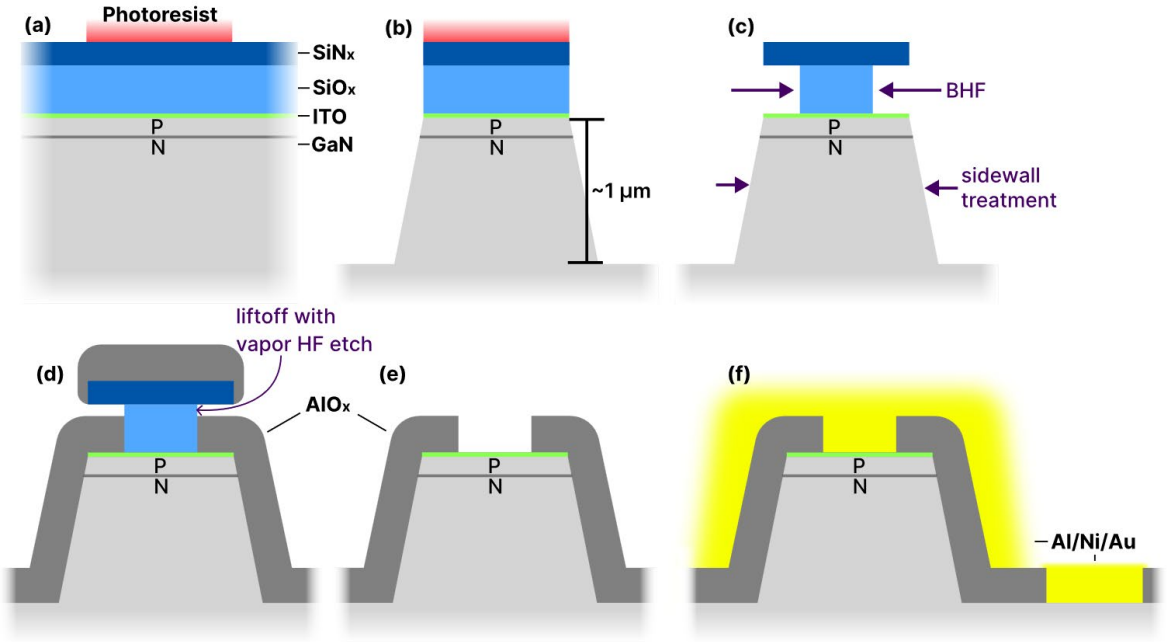



Figure 4-3. Self-aligned fabrication process. Layers are scaled proportionally assuming 1µm diameter mesa and 1µm etch depth. (a) E-beam 30nm ITO, sputter 330nm $SiO_x$, then sputter 170nm $SiN_x$. (b) Dry etch layers from (a) and approximately 1µm into epitaxy. (c) BHF selectively etches $SiO_x$, followed by piranha and KOH (d) Sputter 280nm $AlO_x$. (e) Selective vapor HF etch $SiO_x$ to liftoff. (f) Dry etch n-via through $AlO_x$. Liftoff 600/100/600nm Al/Ni/Au n- and p-pads.

Figure 4-4 shows SEM images throughout the fabrication of a 1µm microLED. The SEM images align with the illustrations in Figure 4-3.

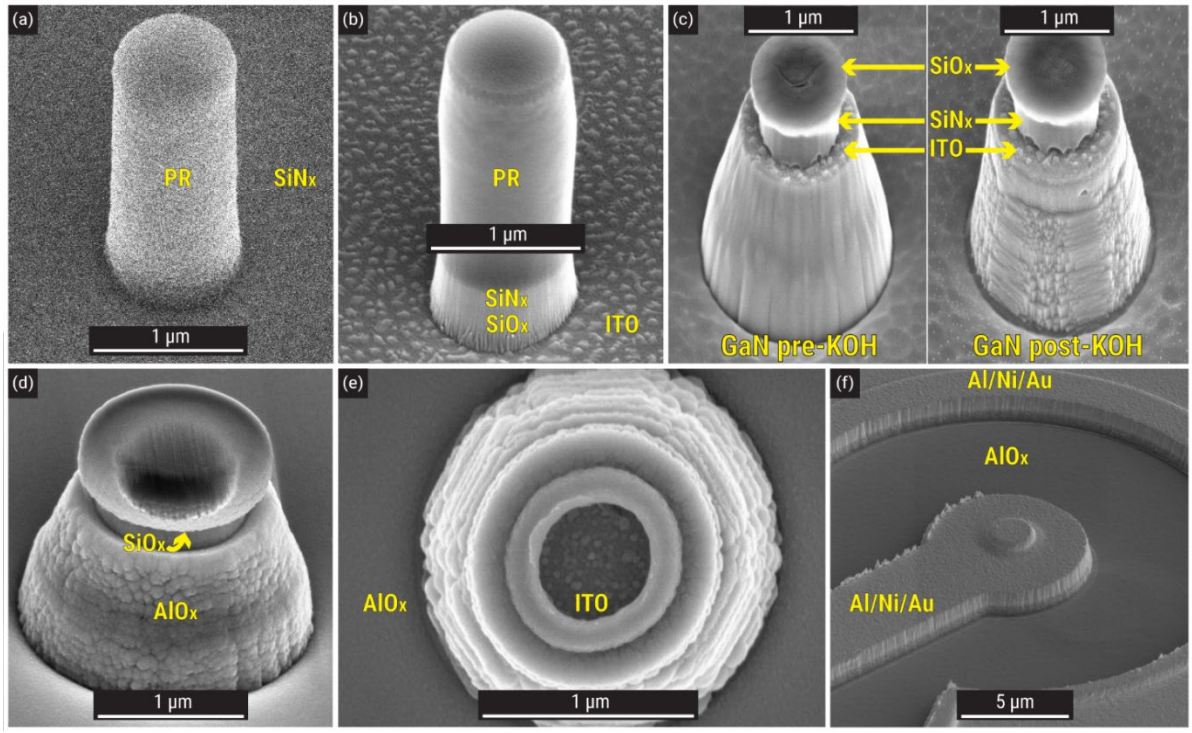



Figure 4-4. SEM micrographs of self-aligned fabrication process of 1µm diameter microLED. Panels (a–f) match Figure 4-3. (a) Pattern photoresist. (b) $SiN_x$/$SiO_x$ layers shown etched prior to etching ITO and LED epitaxy. (c) MicroLED mesa (left) before and (right) after KOH treatment. (d) Deposit $AlO_x$ dielectric. (e) Liftoff using vapor HF etching of $SiO_x$. (f) Deposit pads consisting of 600/100/600 nm Al/Ni/Au.

The process uses standard methods for both deposition and etching of the layers. The most unique tooling needed is vapor HF (step d), although this is standard in micro-electromechanical systems (MEMS) processing. ITO, $SiN_x$, $SiO_x$, (in a), $AlO_x$ (in d) and metal contact layers (in f) are deposited with standard sputter or electron-beam (e-beam) processes. The epitaxy, ITO, $SiN_x$, $SiO_x$ (in b) and $AlO_x$ (in f) are all etched with standard reactive-ion and/or inductively-coupled plasma (ICP) processes.

### 4.3.1 Chemical selectivity

This process is enabled by leveraging the chemical selectivity of the various layers.

The first use of chemical selectivity is (c), where the undercut is formed to later facilitate liftoff. In this case, buffered-HF (BHF) solution is used to selectively etch only the $SiO_2$ layer. Care must be taken that the $SiN_x$ and ITO layers are of high quality, or they may also be etched during this step. The Si/N and Si/O ratios also have a strong effect on the etch rates of the $SiN_x$ and $SiO_x$ layers.

Once the structure in (c) is formed, chemical sidewall treatments, high-temperature activation (for tunnel junctions), or ALD can take place. Since the structure on top is made of dielectrics as opposed to photoresist, it can withstand many harsh chemical treatments. The structure on top is remarkably robust, and remains attached through sonicating, and harsh chemical treatments, such as heated KOH-based etches shown in the next figures.

In (d), vapor HF is used to selectivity etch the $SiO_x$ layer and release the structure in order to open the p-via in (e). Aside from the small area of $SiO_x$ exposed due to the undercut, everything is masked by $AlO_x$, which is inert to vapor HF etching. Tests showed that vapor HF had no effect on the conductivity of the underlying ITO layer.

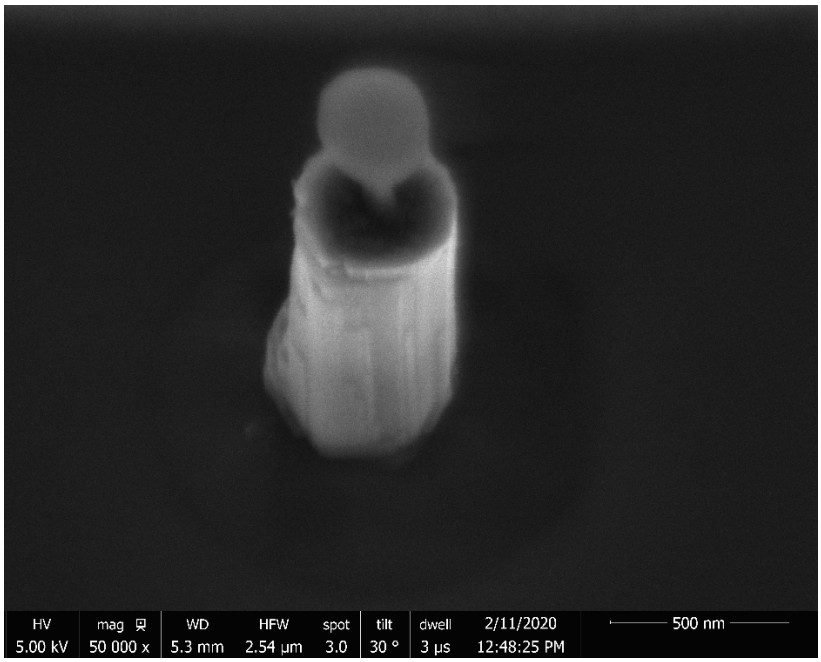



Figure 4-5. 1µm mesa after 20 mins heated (50°C) KOH etching.

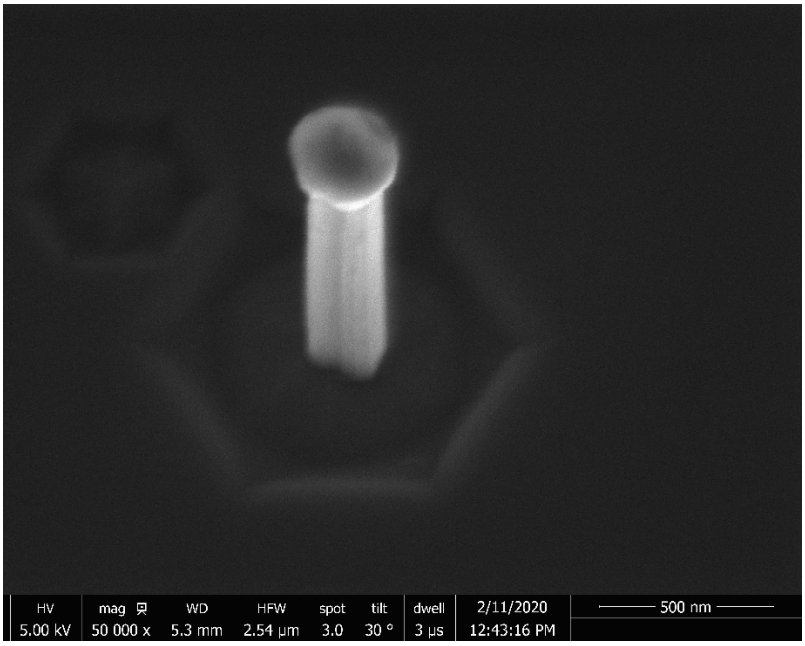



Figure 4-6. 1µm mesa after 40 mins heated (80°C) AZ400k etching.

### 4.3.2 High-density arrays

Unfortunately, we lacked the ability to integrate high-density arrays onto a backplane and create a full display. Still, the process proved to be quite capable in this regard.

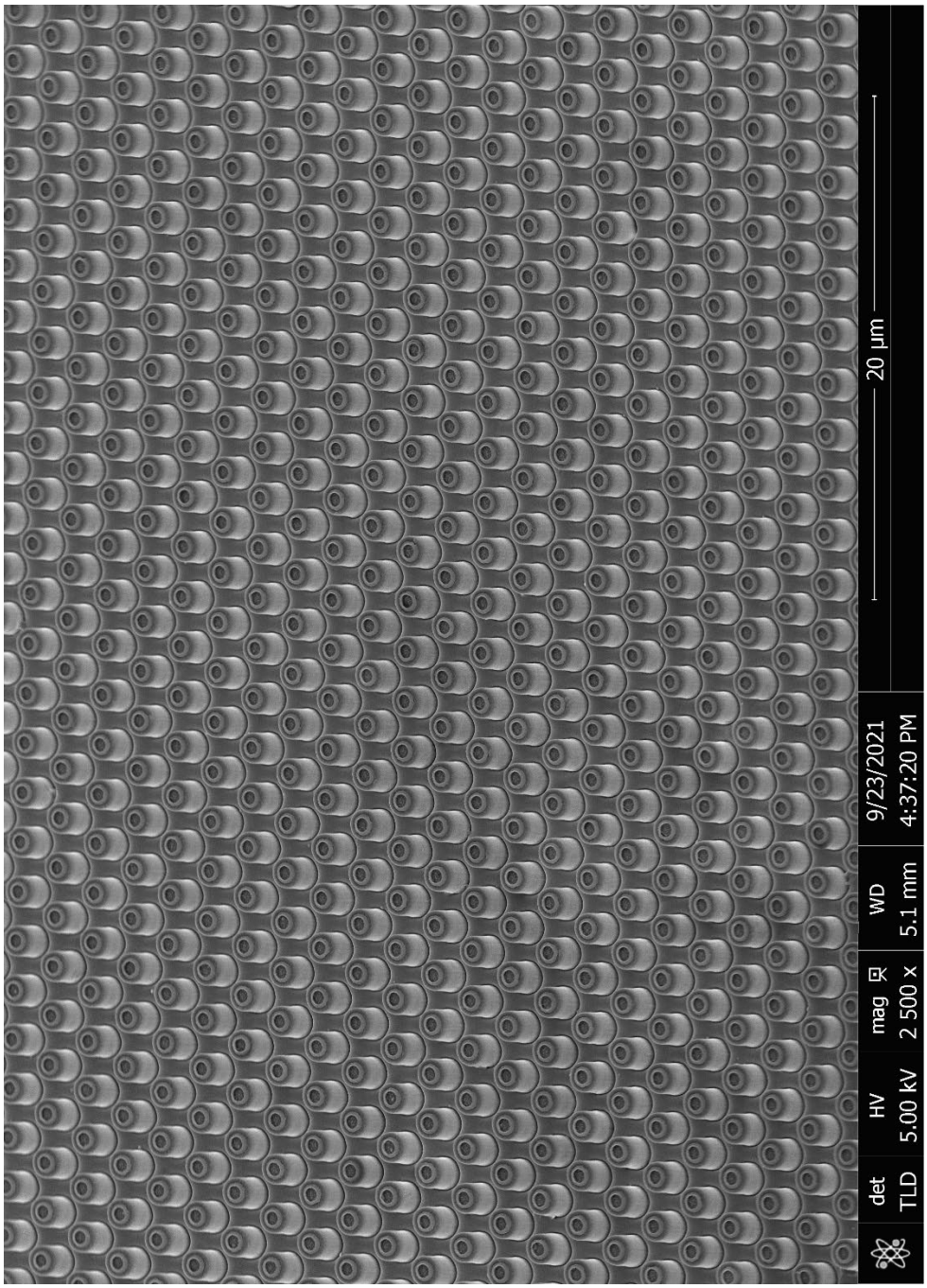



Figure 4-7. 1µm microLED array with 2µm pitch hexagonal packing. Image taken after the liftoff step in Figure 4-3e.

# 5

# Comparison of size-dependent characteristics of blue and green InGaN microLEDs down to 1 micron diameter

The following paper is adapted from

Jordan M. Smith, Ryan Ley, Matthew S. Wong, Yong Hyun Baek, Ji Hun Kang, Chae Hon Kim, Michael J. Gordon, Shuji Nakamura, James S. Speck, Steven P. DenBaars; Comparison of size-dependent characteristics of blue and green InGaN microLEDs down to 1$\mu$m in diameter. *Appl. Phys. Lett.* 18 February 2020; 116 (7): 071102. https://doi.org/10.1063/1.5144819 with the permission of AIP Publishing.

Small formatting changes to the equations and references were made to align better with the rest of this dissertation.

There is growing interest in microLED devices with lateral dimensions between 1 and 10$\mu$m. However, reductions in external quantum efficiency (EQE) due to increased nonradiative recombination at the surface become an issue at these sizes. Previous attempts to study size-dependent EQE trends have been limited to dimensions above 5$\mu$m, partly due to fabrication challenges. Here, we present size-dependent EQE data for InGaN microLEDs down to 1$\mu$m in diameter fabricated using a process that only utilizes standard semiconductor processing techniques (i.e., lithography and etching). Furthermore, differences in EQE trends for blue and green InGaN microLEDs are compared. Green wavelength devices prove to be less susceptible to reductions in efficiency with the decreasing size; consequently, green devices attain higher EQEs than blue devices below 10$\mu$m despite lower internal quantum efficiencies in the bulk material. This is explained by smaller surface recombination velocities with the increasing indium content due to enhanced carrier localization.

MicroLEDs (also known as micro-LEDs, μLEDs) have the potential to replace organic light-emitting diode (OLED) and liquid-crystal display (LCD) technologies in a variety of applications. Compared to LCDs and OLEDs, microLEDs offer many benefits including increased brightness and reliability, reduced power consumption, longer lifetimes, and smaller form factors [92]. Here, we limit the term *microLEDs* to nitride-based or phosphide-based (i.e., InGaN or AlGaInP) devices with dimensions below 100 μm and fabricated via conventional, top-down processing methods; in contrast, terms such as *nanorods*, *nanowires*, and *nanoLEDs* describe devices with dimensions of several micrometers or less and are often fabricated using bottom-up growth techniques.

For most display applications, microLEDs with lateral dimensions below 10 μm will be required to reduce material cost. For example, IHS Research and Veeco predict mesa sizes of 9 μm and 3 μm for 55 in. 4K TVs and smartphones, respectively, which are required to meet cost targets necessary for commercialization [10]. Microdisplays (like those for augmented reality glasses) will also require sizes under 5 μm although the primary driving factors for these displays are high pixel densities and small form factors [7].

Unfortunately, the external quantum efficiency (EQE) of microLEDs decreases as lateral dimensions are reduced [29], [33], [40]. This originates from an increased surface-area-to-volume ratio, which increases nonradiative Shockley–Read–Hall (SRH) recombination at the edge of the mesa. The etched surface contains

crystallographic defects, impurities, and dangling bonds that introduce trap states within the bandgap, which act as nonradiative recombination centers [25], [93].

Size-dependent efficiency in microLEDs can be incorporated into the ABC-model by defining an effective SRH coefficient, which depends on the active region perimeter, $\mathcal{P}$, area, $\mathcal{A}$, surface recombination velocity (SRV), $v_s$, and bulk SRH coefficient, $A_0$,

$$A' = A_0 + v_s \frac{\mathcal{P}}{\mathcal{A}} \qquad \text{Eq. 16}$$

The internal quantum efficiency ($IQE$) becomes

$$IQE = INJ \cdot \frac{Bn^2}{An + Bn^2 + Cn^3} \qquad \text{Eq. 17}$$

In Eq. 17, $n$ is the carrier concentration, $\eta_{inj}$ is the injection efficiency, and $B$ and $C$ are coefficients related to radiative and Auger recombination, respectively. Finally, the $EQE$ is defined as the product of the $IQE$ and light extraction efficiency, $LEE$,

$$EQE = IQE \cdot LEE = \frac{\int_{\lambda_{min}}^{\lambda_{max}} \lambda \cdot \Phi_{e,\lambda}\, d\lambda}{J \cdot \mathcal{A} \cdot \frac{hc}{q}} = \frac{\Phi_e \cdot \langle \lambda \rangle}{J \cdot \mathcal{A} \cdot \frac{hc}{q}} \qquad \text{Eq. 18}$$

The right side of Eq. 18 is used to calculate the $EQE$ from known or measurable quantities: optical power, $\Phi_{e,\lambda}$, centroid wavelength of the electroluminescence (EL) spectrum, $\langle \lambda \rangle$, and current density, $J$ (where $c$, $q$, and $h$ are physical constants). Substituting Eq. 16 and Eq. 17 into Eq. 18 reveals that the $EQE$ is reduced as lateral dimensions decrease in agreement with experimentally observed trends [29], [33], [40].

$$J_{peak} = n_{peak} = \sqrt{\frac{A'}{C}} \qquad \text{Eq. 19}$$

There are no previous reports of microLED EQE trends for mesa dimensions below 5μm, despite commercial demands [92]. This counterintuitive result is partly due to fabrication difficulties that arise at these size ranges; for instance, layer-to-layer alignment for a 1μm microLED becomes intractable using lithography systems available to a typical academic researcher (e.g., aligning a 500 nm dielectric aperture on top of a 1μm mesa). Furthermore, sidewall recombination studies are often convoluted with processing effects, which makes interpreting any observed trends challenging; for example, Olivier *et al.* showed that dry etching the dielectric aperture on top of microLED mesas introduced size-dependent damage to the p-contact, which caused deviations from the EQE trends expected solely from sidewall recombination [30].

A processing scheme (illustrated in Figure 5-1) was developed, which eliminates precise alignments and removes the need to dry etch the dielectric aperture. The core concept is to form a self-aligned undercut structure on top of the mesa (Figure 5-1(c)), which facilitates lift-off of the deposited dielectric to form the aperture and expose indium tin oxide (ITO) for the subsequent electrical contact.

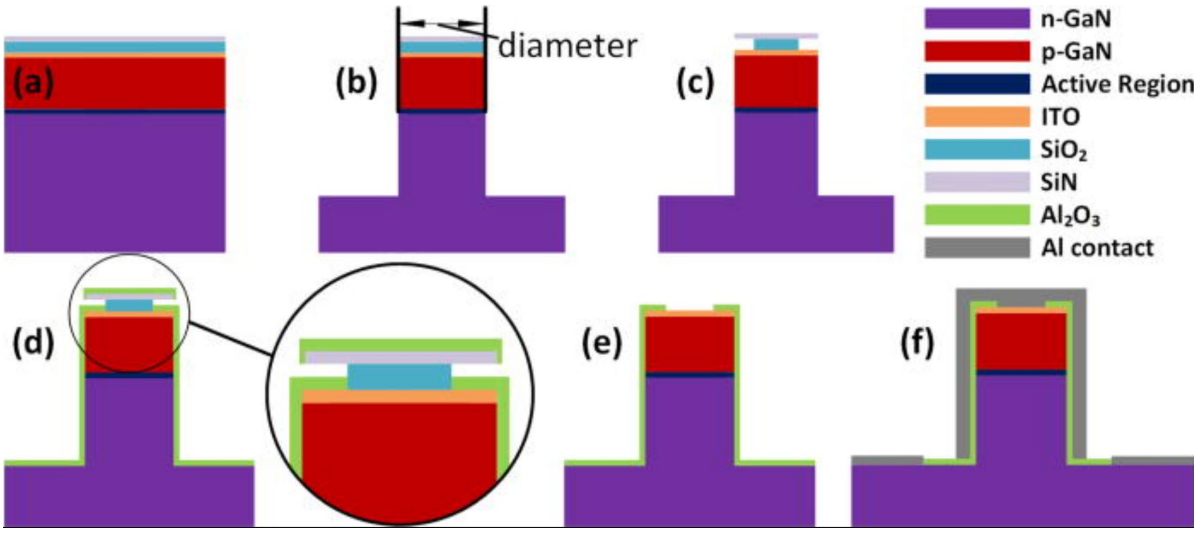



Figure 5-1. Blanket deposition of 30 nm ITO, 300 nm $SiO_2$, and 200 nm SiN on top of the LED epitaxial structure. (b) Dry etch through various layers to define the mesa structure. (c) Selectively undercut $SiO_2$ layer using buffered HF solution. (d) Sputter deposition 250 nm $Al_2O_3$ passivation material. (e) Lift-off by removing the $SiO_2$ layer using vapor HF. (f) Dry etch $Al_2O_3$ to expose n-GaN and deposit reflective 600/100/600 nm Al/Ni/Au common contact/probe-pads via e-beam evaporation and lift-off.

Figure 5-2 shows a scanning electron microscope (SEM) micrograph of a 1μm diameter microLED mesa after the lift-off step corresponding to Figure 5-1(e).

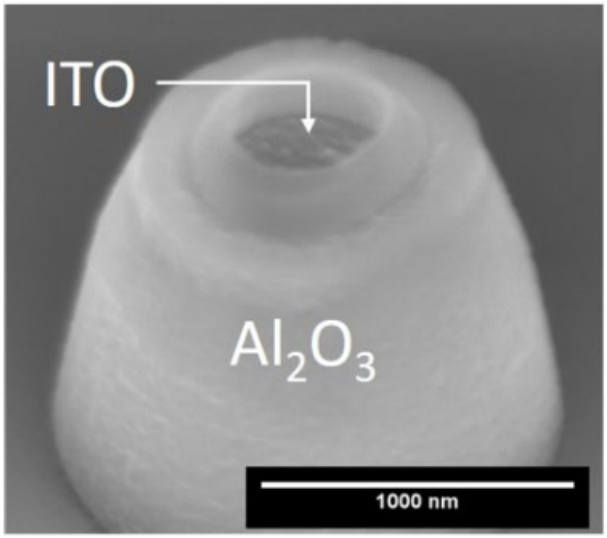



Figure 5-2. SEM micrograph of a 1μm diameter InGaN microLED mesa with Al2O3 dielectric passivation and aperture showing exposed ITO.

The remainder of this paper analyzes the electro-optical characteristics of microLEDs with operating wavelengths of approximately 467nm (blue) and 532nm (green). Devices were fabricated from commercial c-plane epitaxial material grown on sapphire with diameters ranging from 1 to 30μm using the aforementioned process. All devices were processed in parallel to limit any processing variations. For each device size, several devices were tested and their results were averaged, while the error bars indicate the minimum and maximum values measured.

Figure 5-3 compares continuous operation current–voltage characteristics for blue and green devices for device sizes of 1μm and 10μm. When comparing device sizes (for both blue and green) at below-threshold voltages, the 1μm devices exhibit higher current densities as a result of increased surface leakage current [93]. At higher current densities where high injection effects and series resistance dominate, the 1μm and 10μm curves approach similar values, indicating comparable carrier transport across device sizes. This suggests that trends observed in the EQE across device sizes are due to sidewall recombination effects and not related to other processing-related effects such as contact resistance [93].

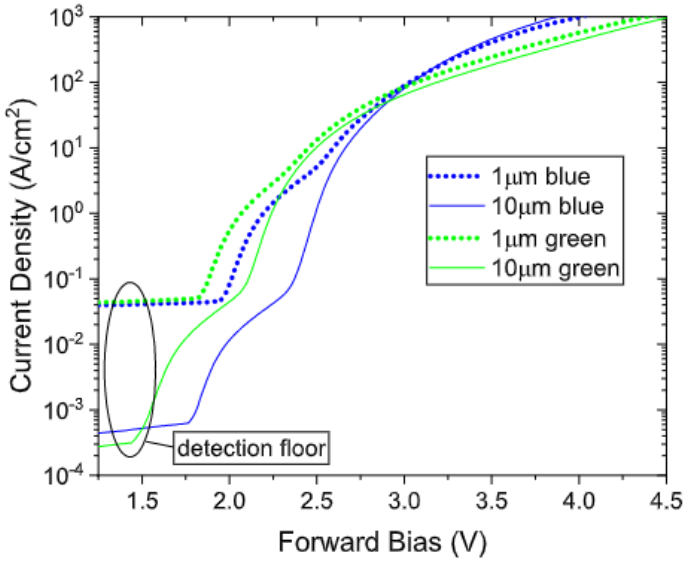



Figure 5-3. Comparison of current-voltage characteristics of 1μm and 10μm diameter devices for blue and green wavelengths.

Optical measurements were conducted on-chip prior to flip-chip bonding or substrate removal. Only light transmitted through the sapphire substrate (downward direction in Figure 5-1) was collected within approximately a 60° half-angle cone normal to the substrate. This geometry was chosen over an integrating sphere as it more accurately imitates how microLEDs are used in displays. However, the limited collection angle caused lower measured EQE values than that would be obtained if the devices were packaged and the total light extracted was collected in an integrating sphere (such as in [33]–[35]). The collection surface was an optical diffuser (Ocean Optics CC-3-DA) coupled to a fiber optic cable. The diffuser's purpose was to make the measured power independent of the incident angle of photon flux, which may vary greatly with the device diameter [49]. The fiber output was collimated and passed through an optional neutral density (ND) filter and focused into a monochromator (Horiba Jovin Yvon iHR320) using a thermoelectrically cooled Synapse CCD detector

to record the electroluminescence (EL) spectra. A fiber-coupled blackbody source (Ocean Optics LS-1-CAL) was used for radiometric calibrations. For each device, EL spectra were measured at various current densities and integrated across all relevant wavelengths to calculate $\Phi_e$ and EQE using Eq. 18.

Figure 5-4 shows measured EQE curves vs current density for devices ranging from 1 to 30 µm in diameter for (a) blue and (b) green wavelengths. The blue wavelength devices show a decrease in efficiency as the size is reduced down to 1 µm as well as a shift in $J_{peak}$ to higher current densities. This result agrees with previously observed EQE trends in blue microLEDs down to 5 µm in size [29], [33], [40] and confirms that there are no deviations in the trend between 1 and 5 µm. The green devices, however, do not follow the same trend, the reason for which is discussed below.

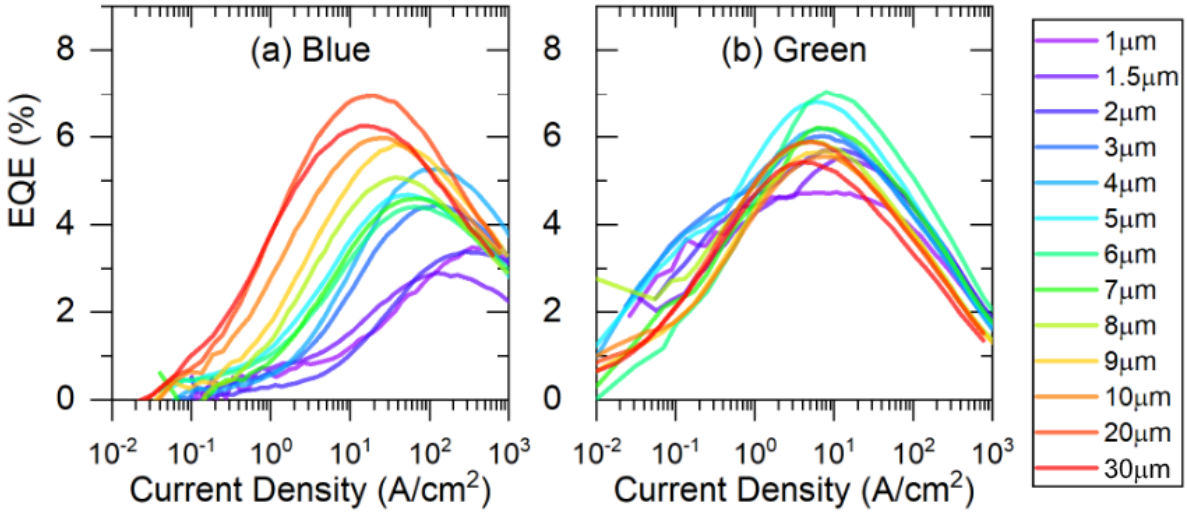



Figure 5-4. EQE vs logarithmic current density for devices 1–30 µm in size for (a) blue and (b) green wavelengths. The results for devices with the highest measured peak EQE are shown (corresponding to the upper ranges in Figure 5-5). EQE values are an underestimate of what would be obtained if devices were packaged and measured in an integrating sphere.

Figure 5-5 plots the peak EQE vs diameter for both blue and green devices, where the upper ranges correspond to the peaks of the EQE curves in Figure 5-4. The EQE remains approximately constant for the larger 10 $\mu$m, 20 $\mu$m, and 30 $\mu$m device sizes for both colors. The EQE clearly begins to reduce at sizes below 10 $\mu$m and 3 $\mu$m for blue and green, respectively. It is clear that the reduction in EQE with the decreasing diameter is less severe for green devices compared to blue. In fact, green devices exhibit higher EQEs than blue devices at diameters below 10 $\mu$m. This crossover is remarkable since it is well-known that the IQE of bulk green InGaN material is lower than that of blue. Many factors contribute to lower IQE in green, including increased defect densities (from increased strain and lower growth temperatures), increased quantum-confined Stark effect (QCSE), and increased Auger recombination due to carrier localization.

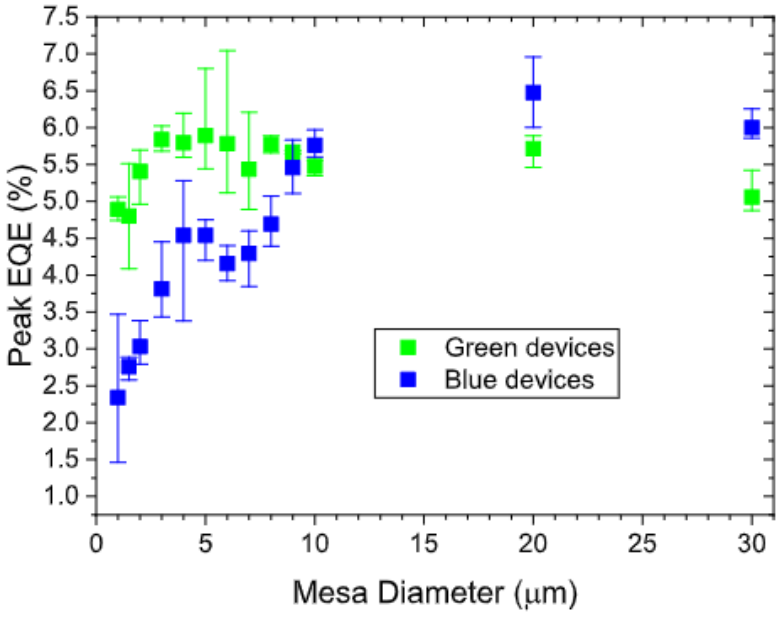



Figure 5-5. Peak EQE is a function of mesa diameter for blue and green devices. Upper ranges correspond to the peaks in Figure 5-4.

The reduced size-dependence of green microLEDs is explained by a smaller SRV, which has been experimentally observed in other InGaN systems [50], [53]. This effect has previously been attributed to increased carrier localization from natural alloy disorder as the indium content is increased [51]–[53], [94]. Eq. 16 reveals that smaller SRV reduces the $\mathcal{P}/\mathcal{A}$ term contribution, resulting in a smaller effective SRH coefficient, A'. This results in a specific diameter where the device set with higher IQE and EQE will crossover from blue to green.

In these particular microLED devices, the EQE crossover between blue and green occurs at 10 $\mu$m; however, the exact crossover diameter will change depending on the device geometry and relative material quality between blue and green. For example, a crossover will exist in bottom-up fabricated axial nanowire LEDs since surface recombination still occurs due to dangling bonds on the nanowire surface. However, the relative values of *SRV*, *LEE*, and ABC-model coefficients between blue and green nanowires would be different from those of the microLEDs discussed here, resulting in the crossover occurring at a different diameter.

Further evidence of reduced surface recombination in green devices is the shift of $J_{peak}$ to significantly lower current densities (note the difference in y-axis scales) in Figure 5-6. This is explainable by a lower A' in Eq. 19 due to a smaller SRV.

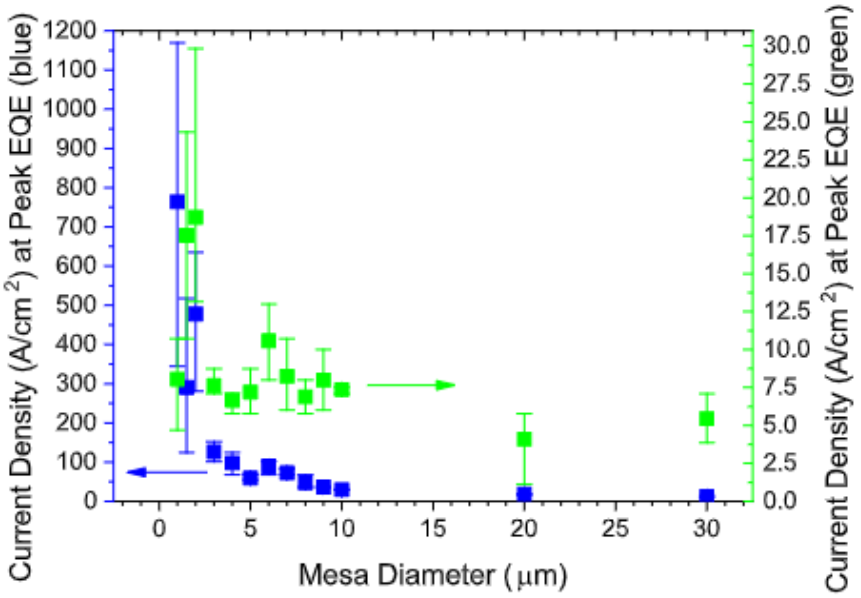



Figure 5-6. Current density at the peak EQE as a function of mesa diameter for blue and green devices.

There is currently some debate as to whether AlGaInP or InGaN should be used as the red light source in microLEDs. The present finding of an EQE crossover in blue and green InGaN microLEDs may have implications in this debate, as an analogous (but more extreme) SRV relationship exists between red AlGaInP and red InGaN microLEDs, respectively. Large-area red AlGaInP emitters typically have much higher IQE values than red InGaN emitters, which suffer from the same issues as green InGaN devices (mentioned previously), but to a greater extent due to the higher indium content. However, the SRV in red AlGaInP is even higher than that in blue InGaN, while the SRV of red InGaN is lower than that of green InGaN [25], [95]. Thus, it is likely that a similar crossover in EQE like the one in Figure 5-5 exists between red AlGaInP and red InGaN microLEDs, where InGaN devices would win out at smaller sizes.

In conclusion, we have achieved electrically injected InGaN microLED devices with diameters down to 1$\mu$m fabricated using conventional, top-down semiconductor processing methods. We also analyzed differences in the size-dependent EQE trends between blue and green wavelength InGaN microLEDs. We have found that the EQE in green wavelength devices exhibits a lessened size-dependence, which is attributed to a reduced SRV due to carrier localization. This results in green devices showing higher EQE values than their blue counterparts for diameters under 10$\mu$m despite lower bulk efficiencies.

This material is based upon the work supported by the National Science Foundation Graduate Research Fellowship under Grant No. 1650114 and funded by the Solid-State Lighting and Energy Electronics Center (SSLEEC) at the University of California, Santa Barbara (UCSB). A portion of this work was performed in the UCSB nanofabrication facility, part of the NSF NNIN network (No. ECS-0335765) and UCSB MRL, which is funded by the NSF MRSEC program (No. DMR-1720256). The authors would like to thank Seoul Viosys for growth of the LED material used in this work.

# 6

# Wavelength- and size-dependent microLED efficiency gain due to reduced surface recombination and enhanced light extraction

## 6.1 Introduction

This study combines the results comparing blue and green microLEDs in [31] (covered previously in Section 5) and light extraction results of [32], and extends them to longer wavelengths. Key figures from those studies are replotted below.

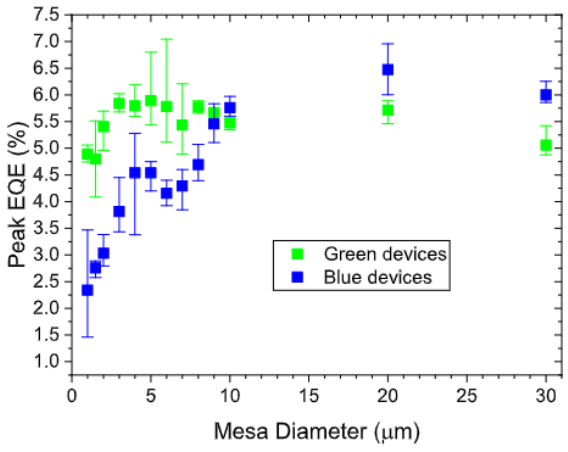



Figure 5-5. Peak EQE is a function of mesa diameter for blue and green devices. Upper ranges correspond to the peaks in Figure 5-4.

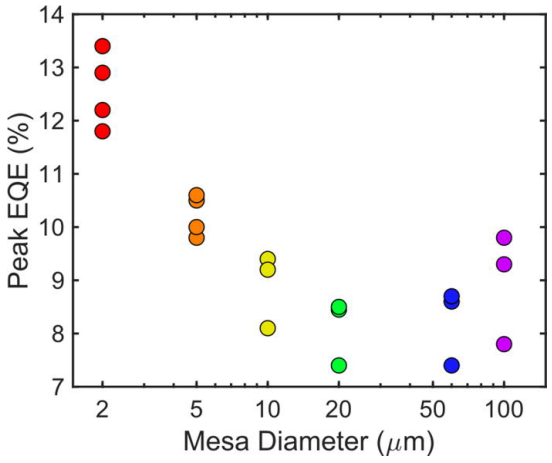



Figure 3-1. Peak EQE versus blue microLED diameter. Reproduced from [32] with the permission of AIP Publishing.

While green devices showed some resistance to size-dependent droop due to surface losses, red devices with higher indium content are expected to exhibit even more resistance due to the higher indium content. If surface recombination is nearly

eliminated (as was achieved in [32] through chemical treatments), then size-dependent EQE gain due to enhanced light extraction at small sizes can be observed.

### 6.1.1 Red InGaN performance

Red InGaN epitaxy suffers from poor bulk internal quantum efficiency (IQE), high voltages, and large spectral dispersion compared to blue and green [96], [97]. Figure 6-1 shows some EQEs for long-wavelength InGaN LEDs compiled by [97].

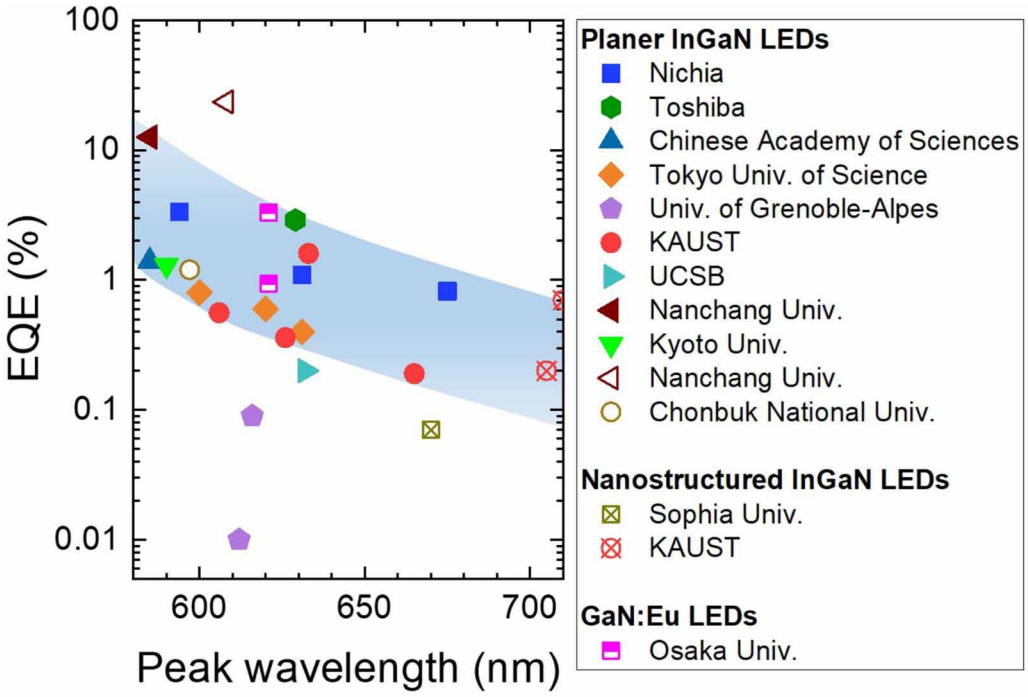



Figure 6-1. EQE of InGaN-based LEDs with peak wavelength ranges from 580 to 710 nm. Solid and open symbols are given by high and low current densities for planar InGaN LEDs and GaN:Eu LEDs. The shaded area indicates the general trend between efficiencies and peak wavelength at standard current density. From [97]. CC-BY 4.0.

### 6.1.2 AR applications

Spectral dispersion causes analagous issues to angular dispersion in AR applications, as both are directly linked to the in-coupler (and out-coupler) grating angle [98]. Emerging metasurfaces could provide an elegant solution to both angular and spectral

dispersion in the form of broadband achromatic optics with large numerical apertures (NA) [99]–[101].

Spectral spread in waveguides for AR can also be partly compensated by using symmetric input and output gratings in opposing directions, as shown in Figure 6-2. Regarding this, Bernard Kress (a leader in AR who worked on Google Glass and Microsoft HoloLens) states [102],

> "This symmetric technique might not be used to compensate for spectral spread across different colors (RGB LEDs) but rather for the spread around a single LED color. The spread across colors might stretch the RGB exit pupils too far apart and reduce the FOV over which all RGB colors can propagate by TIR."

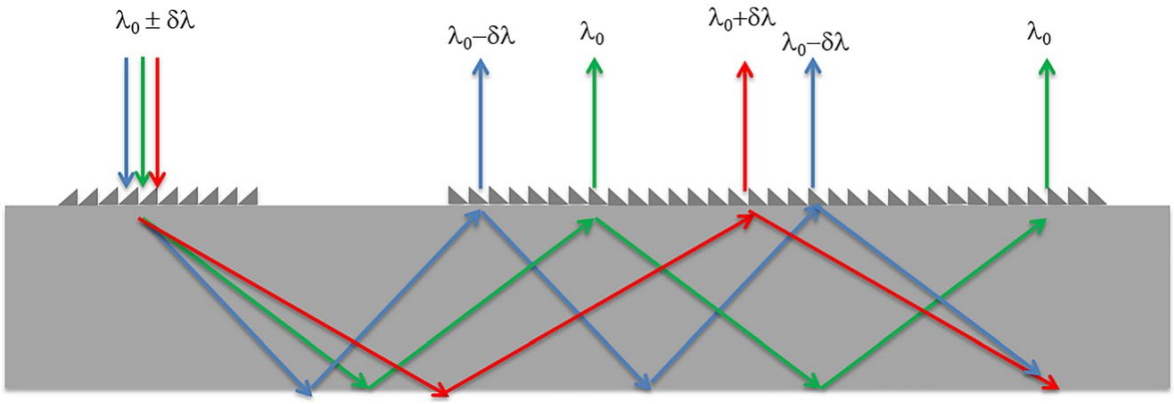



Figure 6-2. Spectral spread compensation in a symmetric in-coupler/out-coupler waveguide combiner. From [102]. CC-BY 4.0.

### 6.1.3 Red alternatives

Due to ongoing challenges in red InGaN, researchers are considering alternative red sources such as AlInGaP (or AlGaInP) [103]–[105] or quantum dot (QD) color conversion layers [106]–[108]. Both red alternatives also have drawbacks. AlInGaP

surface recombination velocity is higher than InGaN, exacerbating size-dependent EQE droop [25], [109]. QDs have degradation issues, add undesirable thickness, and patterning is increasingly challenging as pixel widths drop below 10 μm [110], [111]. In either case, incorporating QDs or AlInGaP adds manufacturing steps that increase complexity and cost compared to an exclusively InGaN RGB microLED display.

### 6.1.4 Growth

LED epitaxial layers are grown via metal-organic chemical vapor deposition (MOCVD) on 2-inch patterned sapphire substrate (PSS). Higher indium concentrations cause longer wavelengths; faster growth rates cause higher indium concentrations [112]. Growth rate and indium concentration decreases from center to edge of the wafer in our reactor [113]. The effects of growth rate and growth temperature are shown in data from [112] in Figure 6-3.

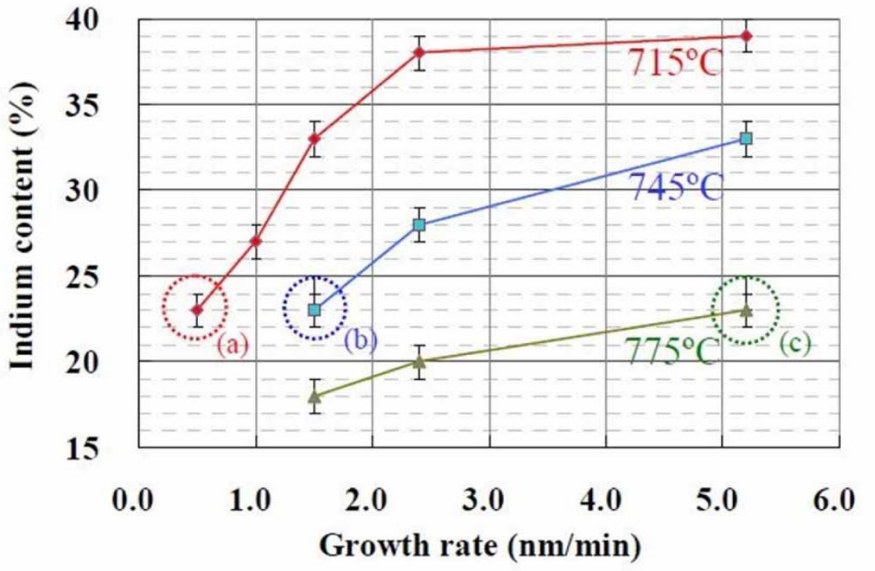



Figure 6-3. Indium content dependence on growth rate at various growth temperatures. Reproduced from [112] with permission from Wiley.

## 6.2 Experimental design and wavelength variation

The operating wavelength at 5 A/cm$^2$ varies between 500–600 nm from edge to center of the wafer. Wavelength nonuniformity is ordinarily undesirable, but here it is intentionally leveraged to study the effects of indium concentration across a single sample; consequently, variations that would occur by processing separate red, green, and blue samples are eliminated.

microLED devices were fabricated using the self-aligned fabrication process introduced in [31]. In contrast to that study, the devices here were also subject to chemical sidewall treatments. The treatment consisted of 2 minutes of Piranha solution (3:1), followed by 15 minutes of KOH (45% w/w, room temperature). This treatment was repeated twice.

The location of the sample diced from a 2 inch wafer is shown in Figure 6-4. Figure 6-4 also shows the location of columns of microLED devices fabricated down the sample and lists the average wavelength of each column at an operating current density of 5 A/cm$^2$ for all device sizes.

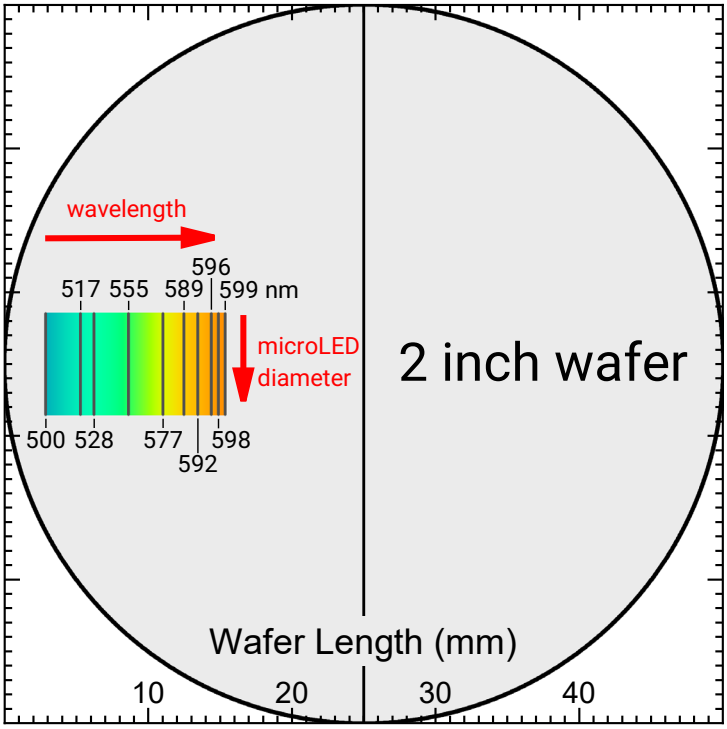



Figure 6-4. Illustration of the (rainbow colored) sample region diced from a 2 inch InGaN epitaxy wafer, grown via MOCVD. Locations of columns of microLEDs of different diameter, as well as the average wavelength of the microLEDs, are shown.

By fabricating the sample in this orientation, microLED size trends (down the vertical-direction of Figure 6-4) can be tested along a gradient of wavelengths (horizontal-direction of Figure 6-4). Instead of the position of each column of microLEDs of varying size, microLED columns/devices will instead be labelled by the average centroid wavelength of each column when devices were tested at 5 A/cm$^2$. Throughout the study, the colors in all the figures attempt to represent the colors emitted by the microLED devices, within the confines of sRGB color space.

Figure 6-5 plots the mean (and standard deviation) centroid wavelength at 5 A/cm$^2$ for each column across the sample. Figure 6-6 plots the data from which the

averages in Figure 6-5 were calculated for each device tested, where the lines connect devices within the same column from Figure 6-4.

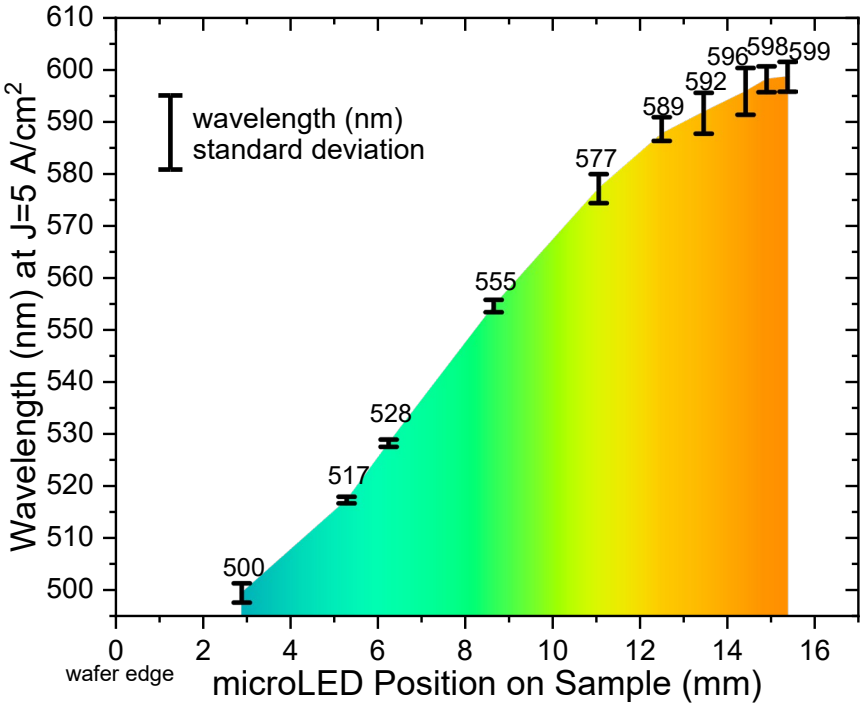



Figure 6-5. Mean centroid wavelength of all devices of differing diameter tested at 5 A/cm$^2$ at different radial positions (in reference to the wafer) along the sample.

Device yield was lower near the central (green) region of the sample, which is presumed to be due to the elongated shape of the sample, which lead to poor photoresist uniformity. Total device yield and available size range was highest in the columns corresponding to 598 nm and 500 nm in Figure 6-5 and Figure 6-6. Since these two sets also represent the extrema of wavelength and indium concentration, they are used throughout the remaining figures.

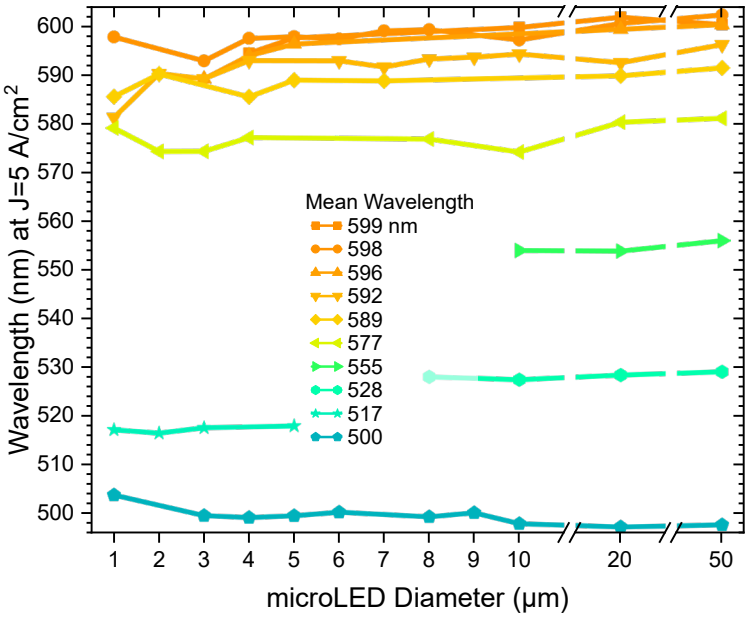



Figure 6-6. Centroid wavelength of microLEDs with diameters ranging from 1–50 μm at an injection current of 5 A/cm$^2$. Lines connect columns of microLEDs occupying the same radial position on a 2 inch InGaN LED epitaxy grown via MOCVD. Each line corresponds to a labeled point in Figure 6-5, which in turn corresponds to a column of microLEDs at similar radial positions on the wafer.

Figure 6-6 shows mostly constant wavelength across device sizes. However, a subtle blueshift at longer wavelengths and smaller device sizes may be present, which could be attributed to strain relaxation [114]–[116].

# 6.3 Results

## 6.3.1 Electrical characteristics

Figure 6-7 plots the current-density versus voltage (JV) of select device sizes from the 500 nm and 598 nm ends of the sample. At the early turn-on stages, the deviation among sizes in current density of the higher wavelength, 598 nm, devices appears lower than that of the 500 nm devices. This would be the expected result if the 598 nm devices had lower surface recombination, and thus lower leakage current.

At higher voltages, the longer wavelength devices exhibit higher series resistance. Higher voltages are commonly observed with increasing indium content, which has been attributed to reduced carrier mobility, resulting from an increased number of alloy scattering centers [117]. However, this issue was also present in the early development of green InGaN LEDs and has been largely overcome in more recent years.

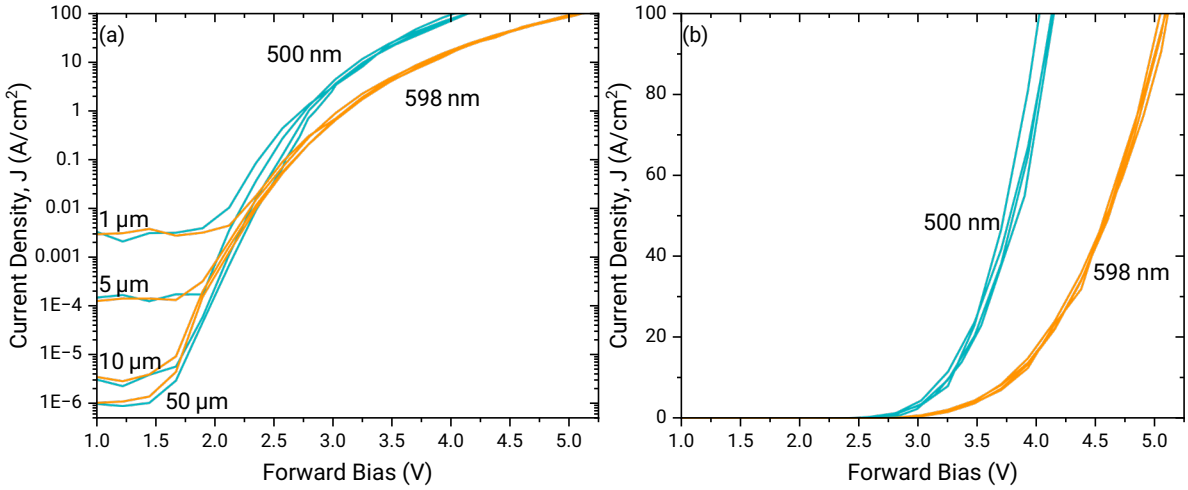



Figure 6-7. (a) Semi-log and (b) linear current-voltage characteristics of 1, 5, 10, and 50 μm microLEDs from sample locations with mean wavelengths of 500 and 598 nm. Voltage-driven.

For either wavelength, JV curves in Figure 6-7 approach similar values at higher bias, independent of device size. This indicates similar series resistance for a given wavelength (or indium concentration), indicating there are no differences in the contact quality across devices sizes; size-dependent series resistance can be a concern if the p-vias of the devices are improperly dry-etched [30], [87], [88].

### 6.3.2 Efficiency

Figure 6-8 shows the peak EQE of all measured devices, with lines connecting devices with mean wavelengths shown in the legend. Beginning with the most-blue, 500 nm, devices, a standard drop in efficiency with decreasing microLED size is observed. On the other extreme, longer-wavelength groupings of device sizes show an opposite increase in EQE as device size decreases. Although yield was low for intermediate wavelengths, the 577 nm grouping of devices appears to have a relatively constant EQE across device sizes.

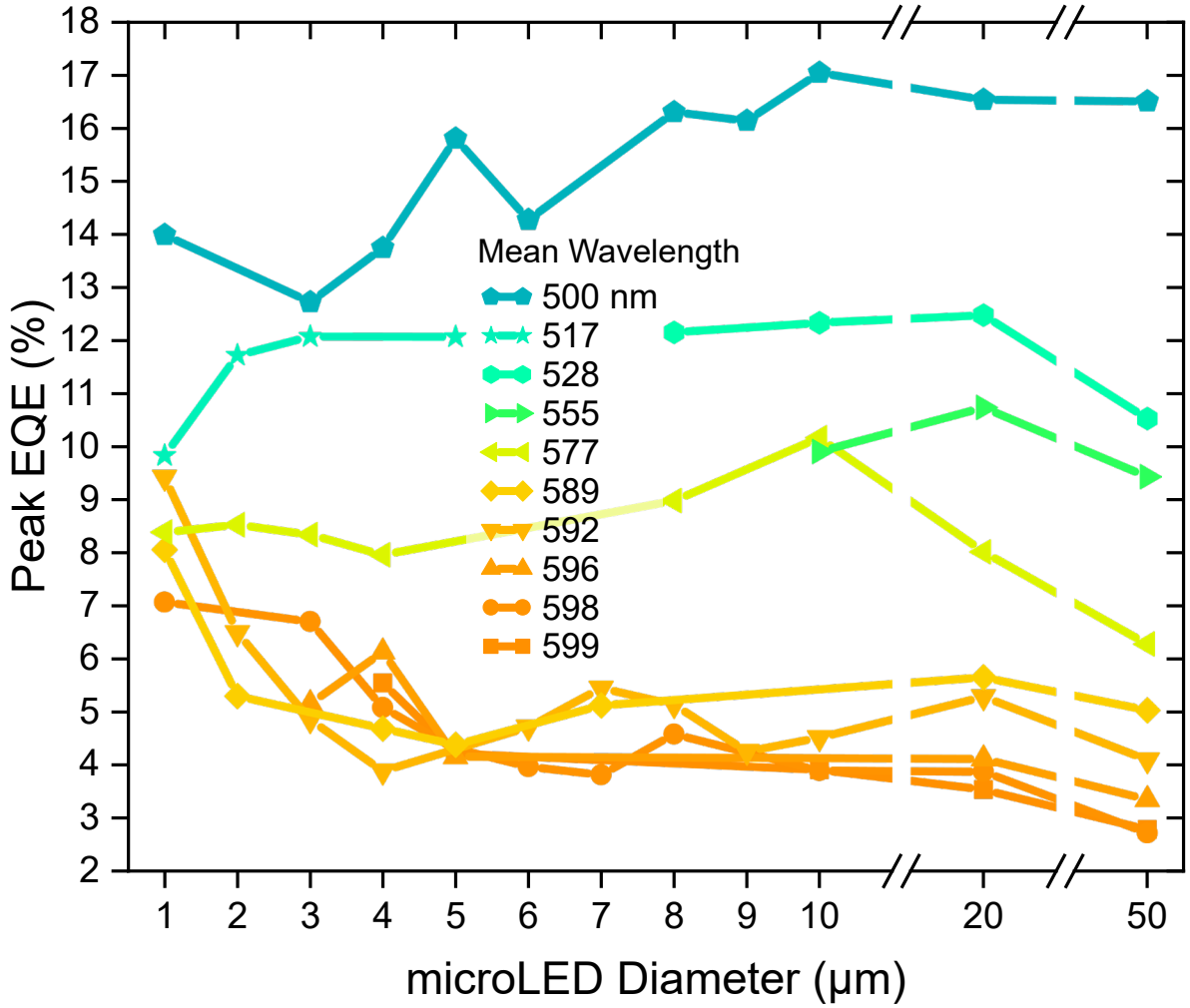



Figure 6-8. Peak external quantum efficiency for all measured devices.

These results, although remarkable, are expected when considering the combination of reduced surface recombination at long wavelengths [31], and increased extraction efficiency at small sizes [32] (see Figure 5-5 and Figure 3-1). In the 500 nm devices, surface recombination is strongest, while in the devices near 600 nm, the surface recombination is lower to due to the lower SRV caused by carrier localization. In other words, there are two opposing size-dependent effects: surface recombination and light extraction enhancement.

Figure 6-9 plots the full EQE versus current density curves for the 500 nm and 598 nm clusters of devices. The peaks of the curves in Figure 6-9 match those plotted in Figure 6-8. The inversion of the peak EQE trend shown in Figure 6-8 is clearly seen here as well.

Since the devices underwent surface treatments, the shift in the peak EQE to higher current densities (Eq. 19) may be reduced even for the bluer devices; however, a small shift of the peak EQE towards higher current densities for smaller devices appears to be present for the 500 nm devices.

Regarding the relative position of the peaks in Figure 6-9 for the 500 nm and 598 nm devices, the longer-wavelength devices peak at a higher current density. This could be attributed to the larger bulk SRH coefficient, $A_0$, (Eq. 15) due to the increased number of crystallographic defects present in longer wavelength epitaxy. This also explains why the longer wavelength devices, in general, show lower overall lower EQE despite the inversion of the size-dependent EQE trend.

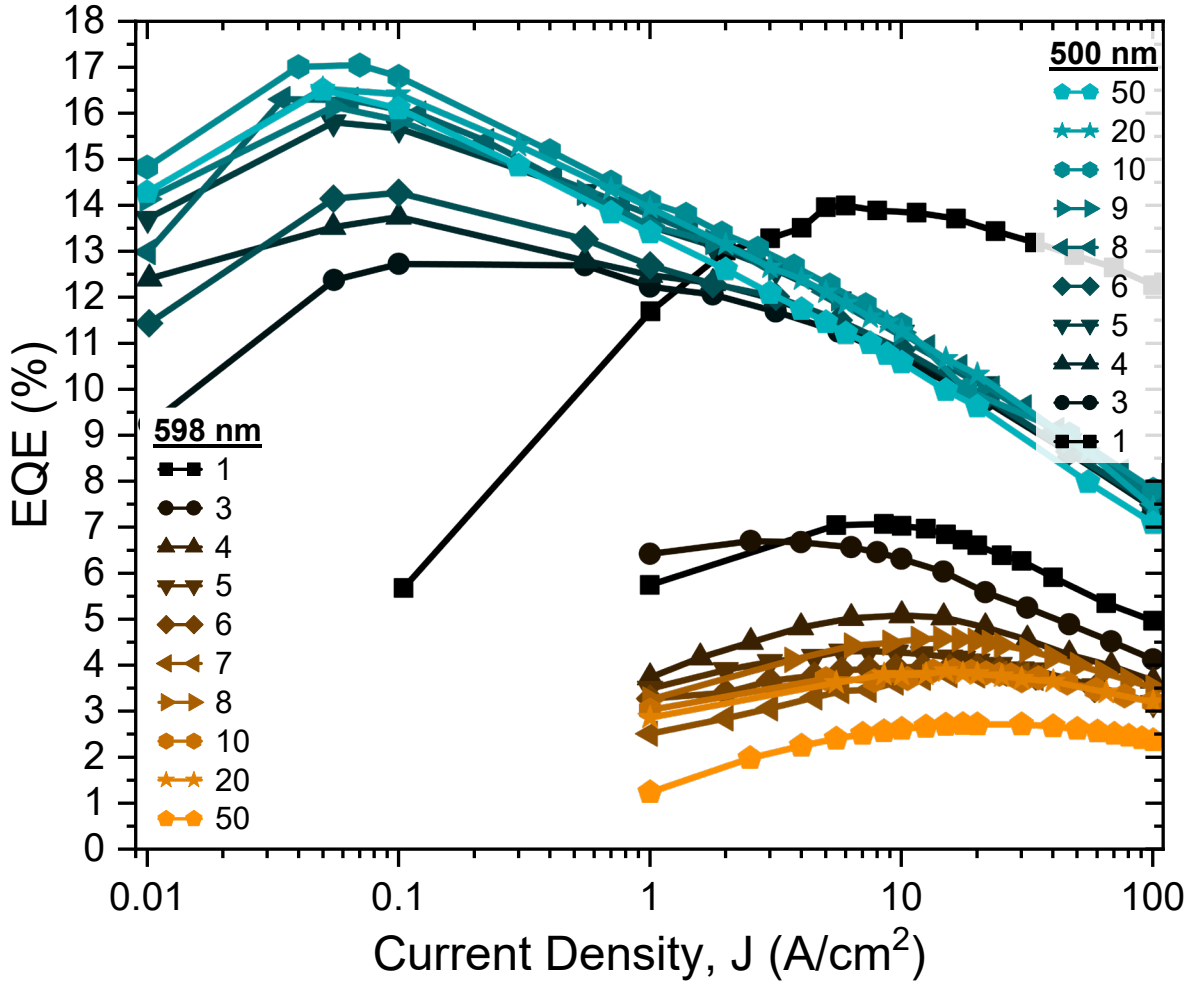



Figure 6-9. Current density versus external quantum efficiency of two sets of devices from opposing ends of the sample, corresponding to different wavelengths and indium concentrations.

### 6.3.3 FDTD simulations

The effects of wavelength (or indium concentration) on size-dependent surface recombination were expected. However, there was concern that the patterned sapphire interface below the devices may also have a wavelength dependence. To rule out that any of the previously observed trends across different wavelengths were the result of the PSS interface, FDTD simulations were carried out.

Figure 6-10 shows a microscope image of the PSS interface beneath a 1μm device, as well as the corresponding FDTD region. The reflectivity of the interface was calculated by injected a plane-wave source into the periodic simulation region, and collecting the fields at the monitor below the patterned interface. The source was swept at angles between 0 to 90 degrees (0 being normal to the interface). For every injection angle, the results were averaged for 2 orientations of the source, corresponding to the principal lattice vectors of a 2D hexagonal lattice. In other words, when the source was pointing directly towards the nearest-neighbor patterned feature, or between the nearest-neighbor towards the next-nearest-neighbor (the latter corresponds to what is seen in the bottom left of Figure 6-10).

The dimensions of the simulation were dictated by the actual shape of the PSS the devices were grown on. Atomic force microscope (AFM) scans provided by the substrate supplier gave this information. The patterning had the shape of a truncated cone. The base diameter and height of the cones were both approximately 420 nm. The pitch was 1μm. The sidewall slope was approximately 38 degrees (0 being vertical).

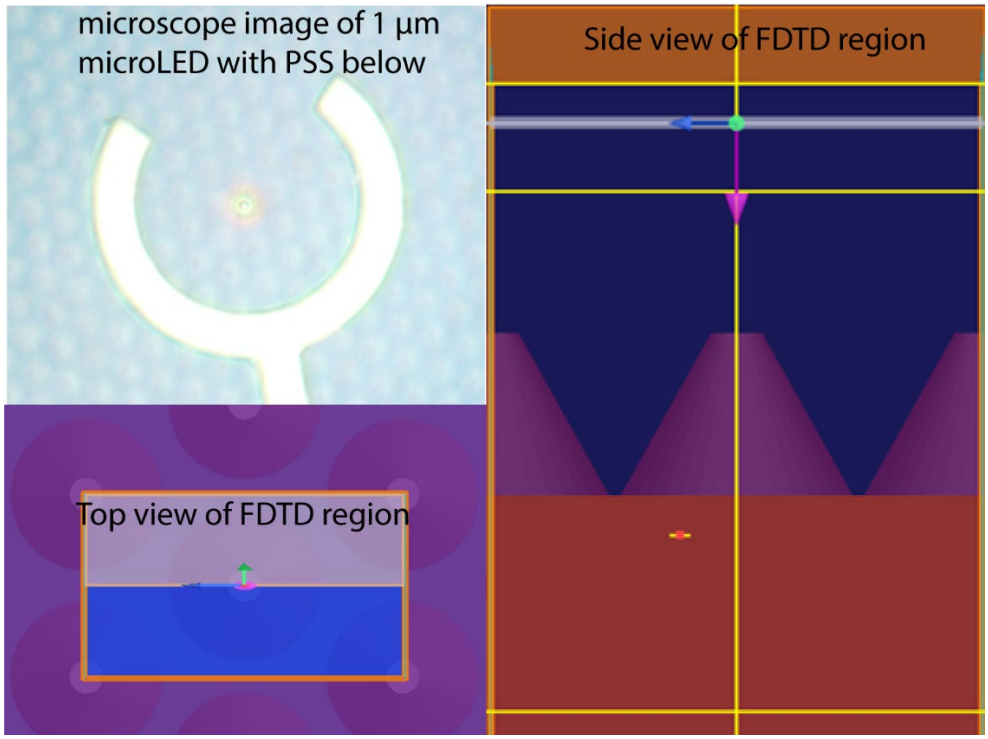



Figure 6-10. Microscope image of 1µm device with PSS pattern below, along with corresponding FDTD region to simulate the reflectivity of the PSS interface.

Figure 6-11 shows the results of the FDTD simulation. Little difference in terms of reflected or transmitted power is seen between wavelengths of 500, 550, or 600 nm. As a reference, the planar interface without patterning was also simulated, which produced a curve with the expected jump in reflectivity beyond the total internal reflection condition (TIR) between GaN/Sapphire. The results show that the patterned interface did not introduce an extraneous wavelength-dependent source of error into the results.

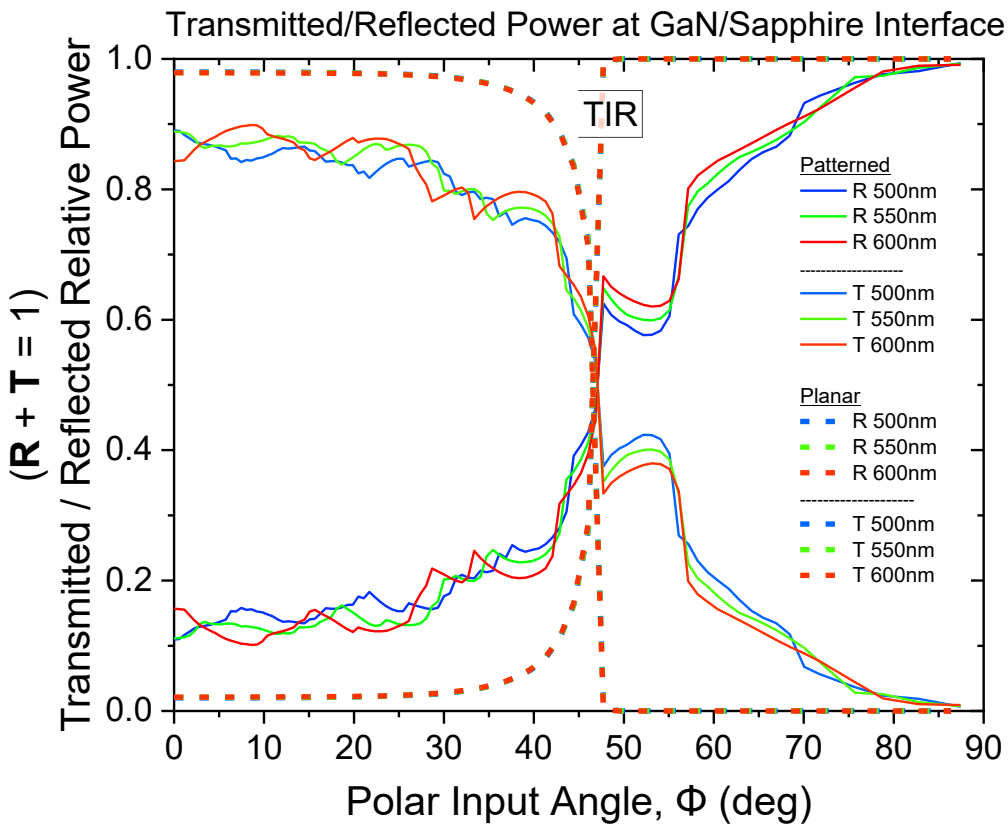



Figure 6-11. FDTD results of the reflectivity of the patterned sapphire interface located below the microLED devices. Results for a planar interface, and the expected total internal reflection features, are also shown.

However, the results do show that the pattern sapphire interface reflects some of the incident power back, even at close-to-normal angles, compared to the planar case. From this, it is reasonable to conclude that the effects of increased directionality are diminished by the presence of PSS. This would reduce the observed increase in efficiency of longer wavelength device (near 600 nm) shown in Figure 6-8. In other words, an even stronger size-dependent increase in efficiency could be expected for the long-wavelength microLEDs if the devices were grown on a planar sapphire substrate. In the case of PSS, some of the light redirected from sidewall reflections

towards the extraction window by small devices was reflected back (roughly 16% or 17% between 0 to 20 degrees).

# 7

# Conclusions

Due to the focus on relatively large devices, at least two additional size-dependent effects in InGaN microLEDs remain understudied: extraction efficiency increases as microLED width decreases, and surface recombination is reduced as indium content increases.

By developing a process to fabricate 1μm microLEDs and fairly compare them to larger devices, the results presented in this dissertation clearly show that size-dependent droop in microLEDs can be counteracted, or even reversed.

The results suggest the detrimental effects of size-dependent droop in microLEDs may be overstated. Future research should explore how to harness the beneficial effects of increased light extraction and resistance to surface recombination in long-wavelength InGaN microLEDs, as opposed to focusing on negating the effects of surface recombination through complex passivation schemes.

The results have also shown that the gap in efficiency between red and blue InGaN is already much smaller than previously believed, once dimensions approach 1μm. Moving towards an entirely InGaN-based microLED display has obvious benefits in terms of cost and simplifies the overall display design. High voltages in red InGaN will need to be addressed to lower the overall wall-plug efficiency. Spectral dispersion

is also a concern, especially for AR, but several approaches to address this issue were discussed in the beginning of Section 6.

# 8

# References


[1] S. Nakamura, T. Mukai, and M. Senoh, "Candela-class high-brightness InGaN/AlGaN double-heterostructure blue-light-emitting diodes," *Appl. Phys. Lett.*, vol. 64, no. 13, pp. 1687–1689, Mar. 1994, doi: 10/drmh43.

[2] C. Weisbuch, S. Nakamura, Y.-R. Wu, and J. S. Speck, "Disorder effects in nitride semiconductors: impact on fundamental and device properties," *Nanophotonics*, vol. 10, no. 1, pp. 3–21, Jan. 2021, doi: 10.1515/nanoph-2020-0590.

[3] Y. Huang, E.-L. Hsiang, M.-Y. Deng, and S.-T. Wu, "Mini-LED, Micro-LED and OLED displays: present status and future perspectives," *Light: Sci. Appl.*, vol. 9, no. 1, p. 105, Jun. 2020, doi: 10/gg3hb2.

[4] Y. Wu, J. Ma, P. Su, L. Zhang, and B. Xia, "Full-Color Realization of Micro-LED Displays," *Nanomaterials*, vol. 10, no. 12, Art. no. 12, Dec. 2020, doi: 10/gmgc7c.

[5] E. H. Virey and Z. Bouhamri, "50-3: Status of MicroLED Mass-Transfer Processes and Equipment," *SID Symp. Dig. Tech. Pap.*, vol. 53, no. 1, pp. 650–653, Jun. 2022, doi: 10/gr28th.

[6] E. H. Virey and Z. Bouhamri, "45-1: Invited Paper: Status of the MicroLED Display Industry," *SID Symp. Dig. Tech. Pap.*, vol. 54, no. 1, pp. 642–645, 2023, doi: 10.1002/sdtp.16640.

[7] E. H. Virey and N. Baron, "45-1: Status and Prospects of microLED Displays," *SID Symp. Dig. Tech. Pap.*, vol. 49, no. 1, pp. 593–596, May 2018, doi: 10/gqt8d7.

[8] E. Virey, "Are MicroLEDs Really the Next Display Revolution?," *Inform. Display*, vol. 34, no. 3, pp. 22–27, May 2018, doi: 10/gr6xhj.

[9] E. H. Virey and Z. Bouhamri, "59-1: *Invited Paper:* From Lab to Fab: Challenges and Requirements for High-Volume MicroLED Manufacturing Equipment," *SID Symp. Dig. Tech. Pap.*, vol. 52, no. 1, pp. 826–829, May 2021, doi: 10/gr29s5.

[10] A. Paranjpe, J. Montgomery, S. M. Lee, and C. Morath, "45-2: *Invited Paper:* Micro-LED Displays: Key Manufacturing Challenges and Solutions," *SID Symp. Dig. Tech. Pap.*, vol. 49, no. 1, pp. 597–600, May 2018, doi: 10/gr6zjv.

[11] K. Ahmed, "Micro LED displays: technology and manufacturing challenges," in *Novel Patterning Technologies 2021*, E. M. Panning and J. A. Liddle, Eds., SPIE, Feb. 2021, p. 41. doi: 10.1117/12.2591107.

[12] R. Chaji, E. Fathi, and A. Zamani, "19-5: *Invited Paper*: Low-Cost Micro-LED Displays for All Applications," *SID Symp. Dig. Tech. Pap.*, vol. 48, no. 1, pp. 264–267, May 2017, doi: 10/gmgc2p.

[13] R. Chaji, E. Fathi, and A. Zamani, "23-1: *Invited Paper:* Essentials of MicroLED Display Production," *SID Symp. Dig. Tech. Pap.*, vol. 51, no. 1, pp. 323–327, Aug. 2020, doi: 10/gr6zgq.

[14] E.-L. Hsiang, Z. He, Y. Huang, F. Gou, Y.-F. Lan, and S.-T. Wu, "Optimal chip size for reducing the power consumption of micro-LED displays," in *Advances in Display Technologies XI*, J.-H. Lee, Q.-H. Wang, and T.-H. Yoon, Eds., SPIE, Mar. 2021, p. 20. doi: 10.1117/12.2578671.

[15] R. T. Ley, "Mitigating Surface Losses and Strain in InGaN MicroLEDs," Ph.D., University of California, Santa Barbara, 2021. Accessed: Sep. 09, 2023. [Online]. Available: https://www.proquest.com/docview/2579961298/abstract/99AB7443E07C43CEPQ/34

[16] J. M. Smith and S. P. DenBaars, "Formation of microled mesa structures with atomic layer deposition passivated sidewalls, a self-aligned dielectric via to the top electrical contact, and a plasma-damage-free top contact," US20220384682A1, Dec. 01, 2022 Accessed: Aug. 16, 2023. [Online]. Available: https://patents.google.com/patent/US20220384682A1/en

[17] H. Cho, D. Kim, S. Lee, C. Yoo, and Y. Sim, "Efficiency enhancement of submicron-size light-emitting diodes by triple dielectric layers," *J. Soc. Inf. Disp.*, vol. 31, no. 5, pp. 289–297, 2023, doi: 10.1002/jsid.1220.

[18] F. Jiang, B.-R. Hyun, Y. Zhang, and Z. Liu, "Role of Intrinsic Surface States in Efficiency Attenuation of GaN-Based Micro-Light-Emitting-Diodes," *Phys. Status Solidi RRL*, vol. 15, no. 2, p. 2000487, 2021, doi: 10.1002/pssr.202000487.

[19] J. Park, W. Baek, D.-M. Geum, and S. Kim, "Understanding the Sidewall Passivation Effects in AlGaInP/GaInP Micro-LED," *Nanoscale Res. Lett.*, vol. 17, no. 1, p. 29, Mar. 2022, doi: 10.1186/s11671-022-03669-5.

[20] T.-Y. Seong and H. Amano, "Surface passivation of light emitting diodes: From nano-size to conventional mesa-etched devices," *Surf. Interfaces*, vol. 21, p. 100765, Dec. 2020, doi: 10.1016/j.surfin.2020.100765.

[21] J.-H. Park *et al.*, "Interplay of sidewall damage and light extraction efficiency of micro-LEDs," *Opt. Lett.*, vol. 47, no. 9, p. 2250, May 2022, doi: 10.1364/OL.456993.

[22] Y.-Y. Li *et al.*, "Analysis of Size-Dependent Quantum Efficiency in AlGaInP Micro–Light-Emitting Diodes With Consideration for Current Leakage," *IEEE Photon. J.*, vol. 14, no. 1, pp. 1–7, Feb. 2022, doi: 10/gsd634.

[23] J. Lång, "53.3: Atomic-scale sidewall passivation for microLED devices," *SID Symp. Dig. Tech. Pap.*, vol. 53, no. S1, pp. 521–524, 2022, doi: 10/gsd63v.

[24] F. Jiang, B.-R. Hyun, Y. Zhang, and Z. Liu, "Role of Intrinsic Surface States in Efficiency Attenuation of GaN-Based Micro-Light-Emitting-Diodes," *Phys. Status Solidi RRL*, vol. 15, no. 2, p. 2000487, Feb. 2021, doi: 10/gngw8n.

[25] K. A. Bulashevich and S. Yu. Karpov, "Impact of surface recombination on efficiency of III-nitride light-emitting diodes," *phys. status solidi (RRL) - Rapid Res. Lett.*, vol. 10, no. 6, pp. 480–484, Jun. 2016, doi: 10/f3mh3t.

[26] S. Wolter *et al.*, "Size-Dependent Electroluminescence and Current-Voltage Measurements of Blue InGaN/GaN μLEDs down to the Submicron Scale," *Nanomaterials*, vol. 11, no. 4, Art. no. 4, Mar. 2021, doi: 10/gr6xjb.

[27] A. Daami and F. Olivier, "InGaN/GaN μLED SPICE modelling with size-dependent ABC model integration," in *Physics and Simulation of Optoelectronic Devices XXVII*, M. Osiński, Y. Arakawa, and B. Witzigmann, Eds., Feb. 2019, p. 13. doi: 10.1117/12.2509382.

[28] W. Tian and J. Li, "Size-dependent optical-electrical characteristics of blue GaN/InGaN micro-light-emitting diodes," *Appl. Opt.*, vol. 59, no. 29, p. 9225, Oct. 2020, doi: 10/gk8xvr.

[29] P. Tian *et al.*, "Size-dependent efficiency and efficiency droop of blue InGaN micro-light emitting diodes," *Appl. Phys. Lett.*, vol. 101, no. 23, p. 231110, Dec. 2012, doi: 10/gjzb6b.

[30] A. Daami, F. Olivier, L. Dupré, F. Henry, and F. Templier, "59-4: *Invited Paper:* Electro-optical size-dependence investigation in GaN micro-LED devices," *SID Symp. Dig. Tech. Pap.*, vol. 49, no. 1, pp. 790–793, May 2018, doi: 10/gr6zgx.

[31] J. M. Smith *et al.*, "Comparison of size-dependent characteristics of blue and green InGaN microLEDs down to 1 $\mu$m in diameter," *Appl. Phys. Lett.*, vol. 116, no. 7, p. 071102, Feb. 2020, doi: 10/gjzb59.

[32] R. T. Ley *et al.*, "Revealing the importance of light extraction efficiency in InGaN/GaN microLEDs via chemical treatment and dielectric passivation," *Appl. Phys. Lett.*, vol. 116, no. 25, p. 251104, Jun. 2020, doi: 10/gp35fh.

[33] D. Hwang, A. Mughal, C. D. Pynn, S. Nakamura, and S. P. DenBaars, "Sustained high external quantum efficiency in ultrasmall blue III–nitride micro-LEDs," *Appl. Phys. Express*, vol. 10, no. 3, p. 032101, Mar. 2017, doi: 10/gr6zhn.

[34] M. S. Wong *et al.*, "High efficiency of III-nitride micro-light-emitting diodes by sidewall passivation using atomic layer deposition," *Opt. Express*, vol. 26, no. 16, p. 21324, Aug. 2018, doi: 10/gk8xvp.

[35] M. S. Wong *et al.*, "Size-independent peak efficiency of III-nitride micro-light-emitting-diodes using chemical treatment and sidewall passivation," *Appl. Phys. Express*, vol. 12, no. 9, p. 097004, Sep. 2019, doi: 10/gp35fj.

[36] P. Tian *et al.*, "Temperature-dependent efficiency droop of blue InGaN micro-light emitting diodes," *Appl. Phys. Lett.*, vol. 105, no. 17, p. 171107, Oct. 2014, doi: 10/gsd65h.

[37] J. Cho, E. F. Schubert, and J. K. Kim, "Efficiency droop in light-emitting diodes: Challenges and counter measures," *Laser Photonics Rev.*, vol. 7, no. 3, pp. 408–421, May 2013, doi: 10/f2d23c.

[38] R. P. Green, J. J. D. McKendry, D. Massoubre, E. Gu, M. D. Dawson, and A. E. Kelly, "Modulation bandwidth studies of recombination processes in blue and green InGaN quantum well micro-light-emitting diodes," *Appl. Phys. Lett.*, vol. 102, no. 9, p. 091103, Mar. 2013, doi: 10/gsd648.

[39] I.-H. Lee *et al.*, "Degradation by sidewall recombination centers in GaN blue micro-LEDs at diameters<30 μm," *J. Alloys Compd.*, vol. 921, p. 166072, Nov. 2022, doi: 10/gr6p5x.
[40] F. Olivier, A. Daami, C. Licitra, and F. Templier, "Shockley-Read-Hall and Auger non-radiative recombination in GaN based LEDs: A size effect study," *Appl. Phys. Lett.*, vol. 111, no. 2, p. 022104, Jul. 2017, doi: 10/gmgbnf.
[41] J.-H. Park, "Toward high performance of micro-LEDs via sidewall engineering for next-generation display."
[42] P. Kirilenko, D. Iida, Z. Zhuang, and K. Ohkawa, "InGaN-based green micro-LED efficiency enhancement by hydrogen passivation of the p-GaN sidewall," *Appl. Phys. Express*, vol. 15, no. 8, p. 084003, Jul. 2022, doi: 10/gsd64x.
[43] Y. Shin *et al.*, "Investigation and direct observation of sidewall leakage current of InGaN-Based green micro-light-emitting diodes," *Opt. Express*, vol. 30, no. 12, p. 21065, Jun. 2022, doi: 10/gr6p6x.
[44] F. Yang *et al.*, "Optical and microstructural characterization of Micro-LED with sidewall treatment," *J. Phys. D: Appl. Phys.*, vol. 55, no. 43, p. 435103, Oct. 2022, doi: 10/gr6p6k.
[45] M. Sheen *et al.*, "Highly efficient blue InGaN nanoscale light-emitting diodes," *Nature*, vol. 608, no. 7921, Art. no. 7921, Aug. 2022, doi: 10/gr78q4.
[46] L. Yu *et al.*, "Ultra-small size (1–20 μm) blue and green micro-LEDs fabricated by laser direct writing lithography," *Appl. Phys. Lett.*, vol. 121, no. 4, p. 042106, Jul. 2022, doi: 10/gr28tg.
[47] J. R. Bonar, G. J. Valentine, Z. Gong, J. Small, and S. Gorton, "High-brightness low-power consumption microLED arrays," presented at the Light-Emitting Diodes: Materials, Devices, and Applications for Solid State Lighting XX, H. Jeon, L.-W. Tu, M. R. Krames, and M. Strassburg, Eds., SPIE, Mar. 2016, p. 97680Y. doi: 10.1117/12.2210931.
[48] H. W. Choi, C. W. Jeon, M. D. Dawson, P. R. Edwards, R. W. Martin, and S. Tripathy, "Mechanism of enhanced light output efficiency in InGaN-based microlight emitting diodes," *J. Appl. Phys.*, vol. 93, no. 10, pp. 5978–5982, May 2003, doi: 10/d2n7dq.
[49] K. Bulashevich, S. Konoplev, and S. Karpov, "Effect of Die Shape and Size on Performance of III-Nitride Micro-LEDs: A Modeling Study," *Photonics*, vol. 5, no. 4, p. 41, Oct. 2018, doi: 10/gr6zgp.
[50] H. Kitagawa, M. Fujita, T. Suto, T. Asano, and S. Noda, "Green GaInN photonic-crystal light-emitting diodes with small surface recombination effect," *Appl. Phys. Lett.*, vol. 98, no. 18, p. 181104, May 2011, doi: 10/cjv3sj.
[51] Y.-R. Wu, R. Shivaraman, K.-C. Wang, and J. S. Speck, "Analyzing the physical properties of InGaN multiple quantum well light emitting diodes from nano scale structure," *Appl. Phys. Lett.*, vol. 101, no. 8, p. 083505, Aug. 2012, doi: 10/gr6zks.
[52] S. F. Chichibu *et al.*, "Origin of defect-insensitive emission probability in In-containing (Al,In,Ga)N alloy semiconductors," *Nat. Mater.*, vol. 5, no. 10, pp. 810–816, Oct. 2006, doi: 10/fhkvdk.

[53] T.-J. Yang, R. Shivaraman, J. S. Speck, and Y.-R. Wu, "The influence of random indium alloy fluctuations in indium gallium nitride quantum wells on the device behavior," *J. Appl. Phys.*, vol. 116, no. 11, p. 113104, 2014, doi: 10/gj7bzf.

[54] B. C. Kress, *Optical architectures for augmented-, virtual-, and mixed-reality headsets*. SPIE, 2020. doi: 10.1117/3.2559304.

[55] "Nanosys shakes the microLED world with glō acquisition - An interview by Yole Developpement - i-Micronews." Accessed: Sep. 19, 2023. [Online]. Available: https://web.archive.org/web/20220703092614/https://www.i-micronews.com/nanosys-shakes-the-microled-world-with-glo-acquisition-an-interview-by-yole-developpement/

[56] "Mojo Vision Rocks the AR World with Red MicroLEDS - IEEE Spectrum." Accessed: Sep. 22, 2023. [Online]. Available: https://spectrum.ieee.org/microled

[57] "JBD demonstrates 2-million nits and 10,000 PPI Micro-LED microdisplays | MicroLED-Info." Accessed: Sep. 22, 2023. [Online]. Available: https://www.microled-info.com/jbd-demonstrates-2-million-nits-and-10000-ppi-micro-led-microdisplays

[58] "Just How Small is the MicroLED Display Engine on Vuzix Next Gen Smart." Accessed: Sep. 19, 2023. [Online]. Available: https://web.archive.org/web/20230920033339/https://www.vuzix.com/blogs/vuzix-blog/just-how-small-is-the-microled-display-engine-on-vuzix-next-gen-smart-glasses

[59] K. Yin, Z. He, J. Xiong, J. Zou, K. Li, and S.-T. Wu, "Virtual reality and augmented reality displays: advances and future perspectives," *J. Phys.: Photonics*, vol. 3, no. 2, p. 022010, Apr. 2021, doi: 10.1088/2515-7647/abf02e.

[60] B. C. Kress, "Waveguide combiner technologies enabling small form factor mixed reality headset architectures," in *Optical Instrument Science, Technology, and Applications II*, R. N. Youngworth, N. Haverkamp, and B. N. Sitarski, Eds., SPIE, Sep. 2021, p. 601. doi: 10.1117/12.2614771.

[61] B. C. Kress and W. J. Cummings, "Optical architecture of HoloLens mixed reality headset," presented at the Digital Optical Technologies 2017, B. C. Kress, W. Osten, and H. P. Urbach, Eds., SPIE, Jun. 2017, p. 103350K. doi: 10.1117/12.2270017.

[62] N. W. Melena and J. T. Wiersma, "Pixel size requirements for AR/MR," in *Optical Architectures for Displays and Sensing in Augmented, Virtual, and Mixed Reality (AR, VR, MR) II*, B. C. Kress and C. Peroz, Eds., SPIE, Mar. 2021, p. 4. doi: 10.1117/12.2584168.

[63] A. Solomashenko, A. Kuznetsov, V. Nikolaev, and O. Afanaseva, "Development of a Holographic Waveguide with Thermal Compensation for Augmented Reality Devices," *Appl. Sci.*, vol. 12, no. 21, Art. no. 21, Jan. 2022, doi: 10.3390/app122111281.

[64] B. C. Kress, “Chapter 8: Invariants in HMD Optical Systems, and Strategies to Overcome Them,” in *Optical architectures for augmented-, virtual-, and mixed-reality headsets*, SPIE, 2020, pp. 77–87. doi: 10.1117/3.2559304.
[65] E. Quesnel *et al.*, “Dimensioning a full color LED microdisplay for augmented reality headset in a very bright environment,” *J. Soc. Inf. Disp.*, vol. 29, no. 1, pp. 3–16, Jan. 2021, doi: 10/gr6xhq.
[66] K. Guttag, “Analyzing Optics’ Pivotal Role in Augmented and Mixed Reality Displays,” *Inform. Display*, vol. 39, no. 2, pp. 20–26, Mar. 2023, doi: 10/gsccr7.
[67] P. Feng *et al.*, “A Simple Approach to Achieving Ultrasmall III-Nitride Microlight-Emitting Diodes with Red Emission,” *ACS Appl. Electron. Mater.*, vol. 4, no. 6, pp. 2787–2792, Jun. 2022, doi: 10/gr6p58.
[68] J. Bai *et al.*, “A Direct Epitaxial Approach To Achieving Ultrasmall and Ultrabright InGaN Micro Light-Emitting Diodes (μLEDs),” *ACS Photonics*, vol. 7, no. 2, pp. 411–415, Feb. 2020, doi: 10/gp35ft.
[69] E.-L. Hsiang, Z. Yang, Q. Yang, P.-C. Lai, C.-L. Lin, and S.-T. Wu, “AR/VR light engines: perspectives and challenges,” *Adv. Opt. Photonics*, vol. 14, no. 4, p. 783, Dec. 2022, doi: 10/gsd636.
[70] L. Baruah, “MicroLED Microdisplays: An Invention Fueled by Augmented Reality,” *Inform. Display*, vol. 38, no. 4, pp. 13–18, Jul. 2022, doi: 10/gsbqw8.
[71] H. W. Choi *et al.*, “GaN micro-light-emitting diode arrays with monolithically integrated sapphire microlenses,” *Appl. Phys. Lett.*, vol. 84, no. 13, pp. 2253–2255, Mar. 2004, doi: 10/fjmfh8.
[72] L. Zhu, P. T. Lai, and H. W. Choi, “An ultraviolet micro-LED array and its application for microlens fabrication,” *phys. status solidi c*, vol. 7, no. 7–8, pp. 2174–2176, 2010, doi: 10/b7n84m.
[73] L. Zhu, P. T. Lai, and H. W. Choi, “Microlens Array on Flip-Chip LED Patterned With an Ultraviolet Micro-Pixelated Emitter,” *IEEE Photon. Technol. Lett.*, vol. 23, no. 15, pp. 1067–1069, Aug. 2011, doi: 10/csc6fs.
[74] W. C. Chong *et al.*, “31.3: Low Optical Crosstalk Micro-LED Micro-Display with Semi-Sphere Micro-Lens for Light Collimation,” *SID Symp. Dig. Tech. Pap.*, vol. 49, no. S1, pp. 339–342, Apr. 2018, doi: 10/gr6xjm.
[75] Z. Fan *et al.*, “Numerical Study on the Light Extraction Efficiency and Angular Energy Distribution of Micro-LEDs,” in *2021 IEEE 6th Optoelectronics Global Conference (OGC)*, Sep. 2021, pp. 267–271. doi: 10.1109/OGC52961.2021.9654366.
[76] H.-Y. Ryu, “Evaluation of Light Extraction Efficiency of GaN-Based Nanorod Light-Emitting Diodes by Averaging over Source Positions and Polarizations,” *Crystals*, vol. 8, no. 1, p. 27, Jan. 2018, doi: 10/gc5f2z.
[77] H.-Y. Ryu, J. Pyo, and H. Y. Ryu, “Light Extraction Efficiency of GaN-Based Micro-Scale Light-Emitting Diodes Investigated Using Finite-Difference Time-Domain Simulation,” *IEEE Photon. J.*, vol. 12, no. 2, pp. 1–10, Apr. 2020, doi: 10/gn826f.
[78] P. P. Maaskant, E. A. O’Carroll, P. M. Lambkin, and B. Corbett, “Light emitting mesa structures with high aspect ratio and near-parabolic sidewalls,”

US7518149B2, Apr. 14, 2009 Accessed: Jun. 24, 2023. [Online]. Available: https://patents.google.com/patent/US7518149B2/en

[79] F. Vögl *et al.*, "Role of pixel design and emission wavelength on the light extraction of nitride-based micro-LEDs," *Opt. Express*, vol. 31, no. 14, pp. 22997–23007, Jul. 2023, doi: 10.1364/OE.489110.

[80] K. A. Bulashevich and S. Yu. Karpov, "Impact of surface recombination on efficiency of III-nitride light-emitting diodes," *physica status solidi (RRL) - Rapid Research Letters*, vol. 10, no. 6, pp. 480–484, Jun. 2016, doi: 10.1002/pssr.201600059.

[81] K. Bulashevich, S. Konoplev, and S. Karpov, "Effect of Die Shape and Size on Performance of III-Nitride Micro-LEDs: A Modeling Study," *Photonics*, vol. 5, no. 4, p. 41, Oct. 2018, doi: 10.3390/photonics5040041.

[82] M. S. Wong *et al.*, "Size-independent peak efficiency of III-nitride micro-light-emitting-diodes using chemical treatment and sidewall passivation," *Applied Physics Express*, vol. 12, no. 9, p. 097004, Sep. 2019, doi: 10.7567/1882-0786/ab3949.

[83] M. Lannoo, "Electron states and recombination velocities at semiconductor surfaces and interfaces," vol. 22, no. 8, pp. 789–795, 1987, doi: 10.1051/rphysap:01987002208078900.

[84] C. G. Van de Walle and D. Segev, "Microscopic origins of surface states on nitride surfaces," *Journal of Applied Physics*, vol. 101, no. 8, p. 081704, Apr. 2007, doi: 10.1063/1.2722731.

[85] D. Segev and C. G. Van De Walle, "Origins of Fermi-level pinning on GaN and InN polar and nonpolar surfaces," *Europhysics Letters*, vol. 76, no. 2, pp. 305–311, Oct. 2006, doi: 10.1209/epl/i2006-10250-2.

[86] N. V. Edwards, M. D. Bremser, T. W. Weeks, R. S. Kern, R. F. Davis, and D. E. Aspnes, "Real-time assessment of overlayer removal on GaN, AIN, and AIGaN surfaces using spectroscopic ellipsometry," *Applied Physics Letters*, vol. 69, no. 14, pp. 2065–2067, Sep. 1996, doi: 10.1063/1.116881.

[87] F. Olivier, S. Tirano, L. Dupré, B. Aventurier, C. Largeron, and F. Templier, "Influence of size-reduction on the performances of GaN-based micro-LEDs for display application," *J. Lumin.*, vol. 191, pp. 112–116, Nov. 2017, doi: 10/gbxnmt.

[88] J.-H. Park *et al.*, "The effect of dry etching condition on the performance of blue micro light-emitting diodes with reduced quantum confined Stark effect epitaxial layer," *J. Appl. Phys.*, vol. 131, no. 15, p. 153104, Apr. 2022, doi: 10.1063/5.0085384.

[89] F. Olivier, S. Tirano, L. Dupré, B. Aventurier, C. Largeron, and F. Templier, "Influence of size-reduction on the performances of GaN-based micro-LEDs for display application," *Journal of Luminescence*, vol. 191, pp. 112–116, Nov. 2017, doi: 10.1016/J.JLUMIN.2016.09.052.

[90] D. Hwang, A. Mughal, C. D. Pynn, S. Nakamura, and S. P. Denbaars, "Sustained high external quantum efficiency in ultrasmall blue III–nitride micro-LEDs," 2017, doi: 10.7567/APEX.10.032101.

[91] J. M. Smith and S. P. DenBaars, "Formation of microled mesa structures with atomic layer deposition passivated SIDEWALLS, a SELF-ALIGNED dielectric via to the top electrical CONTACT, and a PLASMA-DAMAGE-FREE top contact," Application US US17772715 WIPO WO2021086935, Oct. 28, 2019 [Online]. Available: https://patentscope.wipo.int/search/en/detail.jsf?docId=WO2021086935

[92] K. Ding, V. Avrutin, N. Izyumskaya, Ü. Özgür, and H. Morkoç, "Micro-LEDs, a Manufacturability Perspective," *Appl. Sci.*, vol. 9, no. 6, p. 1206, Mar. 2019, doi: 10/gk8xvd.

[93] E. F. SCHUBERT, *Light-Emitting Diodes (3rd Edition).pdf*. Place of publication not identified: E FRED SCHUBERT, 2018.

[94] Y. Narukawa, Y. Kawakami, M. Funato, S. Fujita, S. Fujita, and S. Nakamura, "Role of self-formed InGaN quantum dots for exciton localization in the purple laser diode emitting at 420 nm," *Appl. Phys. Lett.*, vol. 70, no. 8, pp. 981–983, Feb. 1997, doi: 10/b28pkk.

[95] J.-T. Oh *et al.*, "Light output performance of red AlGaInP-based light emitting diodes with different chip geometries and structures," *Opt. Express*, vol. 26, no. 9, p. 11194, Apr. 2018, doi: 10/gngw6p.

[96] P. Li *et al.*, "Progress of InGaN-Based Red Micro-Light Emitting Diodes," *Crystals*, vol. 12, no. 4, p. 541, Apr. 2022, doi: 10/gr6w44.

[97] D. Iida and K. Ohkawa, "Recent progress in red light-emitting diodes by III-nitride materials," *Semicond. Sci. Technol.*, vol. 37, no. 1, p. 013001, Jan. 2022, doi: 10/gp37q3.

[98] H. Mukawa *et al.*, "A full-color eyewear display using planar waveguides with reflection volume holograms," *J. Soc. Inf. Disp.*, vol. 17, no. 3, p. 185, 2009, doi: 10.1889/JSID17.3.185.

[99] J. Xiong, E.-L. Hsiang, Z. He, T. Zhan, and S.-T. Wu, "Augmented reality and virtual reality displays: emerging technologies and future perspectives," *Light: Sci. Appl.*, vol. 10, no. 1, Art. no. 1, Oct. 2021, doi: 10/gm96cd.

[100] M. Pan *et al.*, "Dielectric metalens for miniaturized imaging systems: progress and challenges," *Light: Sci. Appl.*, vol. 11, no. 1, Art. no. 1, Jun. 2022, doi: 10.1038/s41377-022-00885-7.

[101] Z. Li *et al.*, "Meta-optics achieves RGB-achromatic focusing for virtual reality," *Sci. Adv.*, vol. 7, no. 5, p. eabe4458, Jan. 2021, doi: 10.1126/sciadv.abe4458.

[102] B. C. Kress and I. Chatterjee, "Waveguide combiners for mixed reality headsets: a nanophotonics design perspective," *Nanophotonics*, vol. 10, no. 1, pp. 41–74, Oct. 2020, doi: 10.1515/nanoph-2020-0410.

[103] M.-C. Wu, Z.-L. Hsu, and C.-Y. Wu, "High-Pixel-Density 960 × 540 Flip-Chip AlGaInP Red MicroLED Display," *IEEE Trans. Electron Devices*, vol. 69, no. 11, pp. 6206–6211, Nov. 2022, doi: 10/gr6qd9.

[104] M. S. Wong *et al.*, "Improved performance of AlGaInP red micro-light-emitting diodes with sidewall treatments," *Opt. Express*, vol. 28, no. 4, p. 5787, Feb. 2020, doi: 10/gqpzkv.

[105] S. Lan, H. Wan, J. Zhao, and S. Zhou, "Light Extraction Analysis of AlGaInP Based Red and GaN Based Blue/Green Flip-Chip Micro-LEDs Using the Monte Carlo Ray Tracing Method," *Micromachines*, vol. 10, no. 12, p. 860, Dec. 2019, doi: 10/gr6zh2.
[106] T. Ma *et al.*, "Progress in Color Conversion Technology for Micro-LED," *Adv. Mater. Technol.*, vol. 8, no. 1, p. 2200632, Jan. 2023, doi: 10/gr6qfb.
[107] Z. Liu *et al.*, "Micro-light-emitting diodes with quantum dots in display technology," *Light: Sci. Appl.*, vol. 9, no. 1, Art. no. 1, May 2020, doi: 10/gjgj5x.
[108] K.-L. Liang, W.-H. Kuo, H.-T. Shen, P.-W. Yu, Y.-H. Fang, and C.-C. Lin, "Advances in color-converted micro-LED arrays," *Jpn. J. Appl. Phys.*, vol. 60, no. SA, p. SA0802, Jan. 2021, doi: 10/gqpzk2.
[109] M. Boroditsky *et al.*, "Surface recombination measurements on III–V candidate materials for nanostructure light-emitting diodes," *J. Appl. Phys.*, vol. 87, no. 7, pp. 3497–3504, Apr. 2000, doi: 10/cs8xp8.
[110] J. Ryu, S. Park, Y. Park, S. Ryu, K. Hwang, and H. W. Jang, "Technological Breakthroughs in Chip Fabrication, Transfer, and Color Conversion for High-Performance Micro-LED Displays," *Adv. Mater.*, vol. n/a, no. n/a, p. 2204947, Feb. 2023, doi: 10/gr6qfg.
[111] J. Bae *et al.*, "Quantum dot-integrated GaN light-emitting diodes with resolution beyond the retinal limit," *Nat. Commun.*, vol. 13, no. 1, Art. no. 1, Apr. 2022, doi: 10.1038/s41467-022-29538-4.
[112] R. Hashimoto, J. Hwang, S. Saito, and S. Nunoue, "High-efficiency green-yellow light-emitting diodes grown on sapphire (0001) substrates," *phys. status solidi c*, vol. 10, no. 11, pp. 1529–1532, 2013, doi: 10.1002/pssc.201300238.
[113] G. B. Stringfellow, *Organometallic vapor-phase epitaxy: theory and practice*, 2nd ed. San Diego: Academic Press, 1999.
[114] R. C. White *et al.*, "InGaN-Based microLED Devices Approaching 1% EQE with Red 609 nm Electroluminescence on Semi-Relaxed Substrates," *Crystals*, vol. 11, no. 11, p. 1364, Nov. 2021, doi: 10/gsd64w.
[115] S. Keller, S. S. Pasayat, C. Gupta, S. P. DenBaars, S. Nakamura, and U. K. Mishra, "Patterned III-Nitrides on porous GaN: Extending elastic relaxation from the nano- to the micrometer scale," *Phys. Status Solidi RRL*, vol. 15, no. 11, p. 2100234, Nov. 2021, doi: 10/gr6xfk.
[116] R. Ley, L. Chan, P. Shapturenka, M. Wong, S. DenBaars, and M. Gordon, "Strain relaxation of InGaN/GaN multi-quantum well light emitters via nanopatterning," *Opt. Express*, vol. 27, no. 21, p. 30081, Oct. 2019, doi: 10/gqqzsp.
[117] K. Prabakaran *et al.*, "Effects of indium flow rate on the structural, morphological, optical and electrical properties of InGaN layers grown by metal organic chemical vapour deposition," *J. Alloys Compd.*, vol. 811, p. 151803, Nov. 2019, doi: 10.1016/j.jallcom.2019.151803.